FAIRCHILD
S P A C E

FSC-ESD-217-93-519

RADIOISOTOPE THERMOPHOTOVOLTAIC (RTPV) GENERATOR AND ITS APPLICATION TO THE PLUTO FAST FLYBY MISSION

A. Schock
M. Mukunda
T. Or
V. Kumar
G. Summers

Fairchild Space and Defense Corporation
Germantown, MD 20874

January 16, 1994

RADIOISOTOPE THERMOPHOTOVOLTAIC (RTPV) GENERATOR AND ITS APPLICATION TO THE PLUTO FAST FLYBY MISSION

A. Schock
M. Mukunda
T. Or
V. Kumar
G. Summers

Abstract

The paper describes the results of a DOE-sponsored design study of a radioisotope thermophotovoltaic generator. Instead of conducting a generic study, it was decided to focus the design effort by directing it at a specific space mission, Pluto Fast Flyby (PFF). That mission, under study by JPL, envisages a direct eight-year flight to Pluto (the only unexplored planet in the solar system), followed by comprehensive mapping, surface composition, and atmospheric structure measurements during a brief flyby of the planet and its moon Charon, and transmission of the recorded science data to Earth during a one-year post-encounter cruise.

Because of Pluto's long distance from the sun (30-50 A.U.) and the mission's large energy demand, JPL has baselined the use of a radioisotope power system for the PFF spacecraft. The chief advantage of Radioisotope Thermophotovoltaic (RTPV) power systems over current Radioisotope Thermoelectric Generators (RTGs) is their much higher conversion efficiency, which greatly reduces the mass and cost of the required radioisotope heat source. Those attributes are particularly important for the PFF mission, which - like all NASA missions under current consideration - is severely mass- and cost-limited.

The paper describes the design of the radioisotope heat source, the thermophotovoltaic converter, and the heat rejection system; and presents the results of the thermal, electrical, and structural analysis and the design optimization of the integrated RTPV system. It briefly summarizes the RTPV system's current technology status, and lists a number of factors that may greatly reduce the need for long-term tests to demonstrate generator lifetime. Our analytical results show very substantial performance improvements over an RTG designed for the same mission, and suggest that the RTPV generator, when developed by DOE and/or NASA, would be quite valuable not only for the PFF mission but also for other future missions requiring small, long-lived, low-mass generators.

INTRODUCTION

Major changes are occurring in the field of space technology. For budgetary and other reasons, there is a strong drive for cheaper and quicker space science missions, partly through use of smaller and lighter spacecraft and their components. Among those components is the power system, which typically represents a major fraction of the cost and mass of the spacecraft.

For powering small, long-duration spacecraft, there are two types of power sources: solar and nuclear (specifically radioisotope systems, since nuclear reactors are too large and massive for small spacecraft). Whenever they have a choice, mission designers prefer solar power systems, because of their lower cost and simpler launch approval process. But they don't always have a choice, because there are applications which may be too far from the sun or at high planetary latitudes or dust-obstructed locations with too little sunlight for effective solar power generation. For those applications, radioisotope power sources may be most attractive or even enabling (e.g., Apollo, Pioneer 10/11, Voyager, Viking, Galileo, Ulysses, Cassini).

But present radioisotope thermoelectric generators (RTGs) are quite costly, because of the high cost of radioisotope heat sources and the low efficiency (~7%) of thermoelectric conversion systems. To reduce the cost of radioisotope power systems, it is necessary to achieve major increases in conversion efficiencies in order to diminish the number of costly heat source modules needed for a given application. Fortunately, there are a number of advanced conversion systems that may be able to triple the conversion efficiency of present thermoelectric converters. These include the Stirling [1], AMTEC [2], and the thermophotovoltaic (TPV) [3] options. The latter is the basis of the design study described in the present paper.

The TPV concept is an outgrowth of progress on photovoltaic (PV) solar cells. In solar systems, the photovoltaic cells convert solar radiation into electricity, while in TPV systems they convert infrared radiation emitted by a hot surface. If the hot surface is heated by a radioisotope heat source, the resultant system is referred to as a radioisotope thermophotovoltaic (RTPV) generator. This concept had been recognized for some time, but until recently the available materials did not permit competitive efficiencies.

Since the infrared spectrum at reasonable temperatures peak at a very different wavelength than the solar spectrum, TPV systems require photovoltaic cells with significantly different band gap energies. Conventional PV materials, like silicon or gallium arsenide (GaAs), would be quite inefficient in TPV devices. But gallium antimonide (GaSb) or gallium-indium antimonide have spectral properties that make them attractive candidates for TPV applications. This was recognized by Boeing personnel, who had been investigating GaSb cells in back of conventional GaAs cells, to produce a tandem solar cell which in their experiments yielded efficiencies up to 35%, significantly higher than plain GaAs cells [4]. The high efficiencies of the tandem cells derive from the spectral characteristics of GaSb, which enable it to utilize the wavelengths that pass through the GaAs cells. These same characteristics make GaSb attractive for TPV applications.

Boeing personnel also recognized that the efficiency of the TPV system could be greatly improved by interposing a spectrally selective filter between the hot surface and the GaSb cell. The filter is designed to transmit those wavelengths that can be efficiently converted to electricity by GaSb, and to reflect other wavelengths back to the heat source, to conserve energy. It is the filter that makes possible the high efficiencies currently projected for TPV systems.

The present paper deals with the design and thermal, electrical, and structural analyses of an integrated system consisting of a radioisotope heat source, an array of TPV converter cells, and an optimized radiator for rejecting the waste heat to space. As will be seen, the integrated RTPV system - when successfully developed - has attributes that would make it an excellent candidate as a lighter and cheaper replacement for present RTGs. Thus, it could be applied to a number of potential missions. But to focus the present design study, it was decided to design an RTPV generator for a specific application, the Pluto Fast Flyby (PFF) mission, which is an excellent example of the trend towards smaller, lighter, and cheaper spacecraft and subsystems [5].

Pluto is the only unexplored planet in the solar system, and there is great scientific interest in a spacecraft reconnaissance of the planet and its large moon Charon, before the atmosphere of Pluto condenses as it recedes from the sun [6]. As its name implies, the Pluto Fast Flyby mission under study by JPL for NASA contemplates a spacecraft to "fly by" the planet rather than to orbit or land on it. This simplification permits major size, mass, and cost reductions, and greatly shortens the time for development of the spacecraft and for transit to Pluto. JPL is considering a launch around the year 2000, with two direct eight-year flights to Pluto (no gravity assist). The science data recorded during the brief Pluto flyby, including visual, infrared, ultraviolet, and radio observations of both sides of the planet/moon system, would then be transmitted to Earth during a one-year post-encounter cruise.

JPL's power demand schedule for the baseline PFF mission called for a peak (including 20% contingency) of 63 watts(e) at the end of the 9.2-year mission. At a distance of 30 or more astronomical units from the sun, the incident solar-flux is at least three orders of magnitude lower than at Earth, which would require very large solar arrays. In fact, it is unclear whether current solar arrays would function at Pluto at all, because of still unsolved Low-Intensity, Low-Temperature (LILT) effects on solar arrays. Therefore, JPL's baseline design called for the use of a radioisotope power source for PFF [7].

The spacecraft size reduction made possible by the flyby mission plan is illustrated in Figure 1, which compares the size of an early (1992) JPL baseline design with the much larger spacecraft of preceding RTG-powered interplanetary missions (Voyager, Galileo, Cassini). That PFF baseline design had an estimated mass (including propellant) of 165 kg, with a mass reduction goal to 112 kg. This implied a 47% mass reduction of the radioisotope power source, from 17.8 kg to 9.5 kg, clearly a very formidable goal.

Fig. 1 Comparative Size of PFF and Prior Spacecraft

VOYAGER   GALILEO   CASSINI   PLUTO FLYBY

3
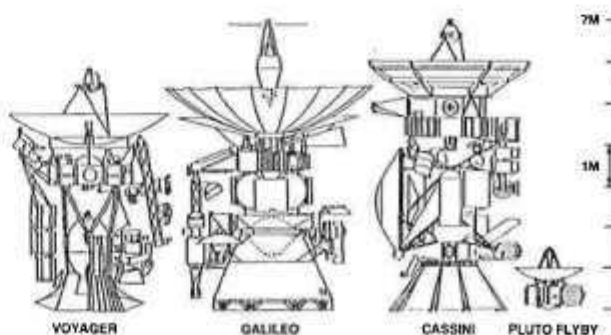
To support NASA and JPL, the Department of Energy's Radioisotope Power Systems Division commissioned Fairchild Space and Defense Corporation under Contract DE-AC01-93-32177 to prepare conceptual designs for a variety of PFF power source options, to help clarify the available options and to provide reliable mass estimates and technology status assessments. The study results are designed to support informed trade-off decisions by program management. Eight options were designed, analyzed, and reported on last year: five thermoelectric [8] and three Stirling systems [9]. None of these (except for a non-redundant Stirling system option) achieved the desired mass reduction goal. Since then, Fairchild has conducted a similar study, reported here, which showed that that goal can be achieved and substantially surpassed with an RTPV system. We are also planning to do a similar study of an isotope-heated AMTEC system. .

TPV CONVERTER ANALYSIS

This section presents a generic analysis of the thermophotovoltaic energy conversion process, not tied to any specific converter geometry or heat source thermal power. The equations derived in this section will be applied to specific geometries in subsequent sections.

The emitted heat flux in the wavelength interval λ to $\lambda + d\lambda$ from a black body at absolute temperature T is given by

$$q(\lambda)d\lambda = \frac{2\pi hc^2\lambda^{-5}d\lambda}{\exp(hc/\lambda kT)-1,} \tag{1}$$

where h and k are Planck's and Boltzmann's constants and c is the speed of light.

For a planar heat source S separated by a vacuum gap from a parallel planar converter C, the spectral energy flux leaving each surface is given by the sum of the emitted and reflected radiation:

$$q_s(\lambda)d\lambda = \varepsilon_s(\lambda)\frac{2\pi hc^2\lambda^{-5}d\lambda}{\exp(hc/\lambda kT_s)-1} + R_s(\lambda)q_c(\lambda)d\lambda, \tag{2}$$

$$q_c(\lambda)d\lambda = \varepsilon_c(\lambda)\frac{2\pi hc^2\lambda^{-5}d\lambda}{\exp(hc/\lambda kT_c)-1} + R_c(\lambda)q_s(\lambda)d\lambda, \tag{3}$$

where $\varepsilon(\lambda)$ and $R(\lambda)$ are the respective surface's spectral emissivity and reflectivity at wavelength λ.

The net radiative heat flux $q(\lambda)$ $d\lambda$ emitted by the heat source and absorbed by the converter in the wavelength interval λ to $\lambda + d\lambda$ is given by

$$q(\lambda)d\lambda = [q_s(\lambda) - q_c(\lambda)]d\lambda. \tag{4}$$

4

Solving Eqs. (2) and (3) for $q_S(\lambda)$ and $q_C(\lambda)$ and inserting the results into Eq. (4), we obtain

$$q(\lambda)d\lambda = \frac{2\pi hc^2\lambda^{-5}}{1-R_s(\lambda)R_c(\lambda)}\left[\frac{\varepsilon_s(\lambda)[1-R_c(\lambda)]}{\exp(hc/\lambda kT_s)-1} - \frac{\varepsilon_c(\lambda)[1-R_s(\lambda)]}{\exp(hc/\lambda kT_c)-1}\right]d\lambda. \tag{5}$$

Since $T_C \ll T_S$ in the present case, the second term in the square bracket is negligible, and Eq. (5) reduces to

$$q(\lambda)d\lambda = \frac{2\pi hc^2\lambda^{-5}}{1-[1-\varepsilon_s(\lambda)]R_c(\lambda)}\left[\frac{\varepsilon_s(\lambda)[1-R_c(\lambda)]}{\exp(hc/\lambda kT_s)-1}\right]d\lambda, \tag{6}$$

which can be further reduced to

$$q(\lambda)d\lambda = \frac{2\pi hc^2\lambda^{-5}[\exp(hc/\lambda kT_s)-1]^{-1}}{[\varepsilon_s(\lambda)]^{-1}+\{[R_c(\lambda)]^{-1}-1\}^{-1}}d\lambda. \tag{7}$$

Note that the converter reflectivity $R_c(\lambda)$ includes the effect of the spectrally selective filter, which plays a major role in determining the system efficiency of the generator.

The energy flux absorbed by the converter is in the form of photons. Since each photon has an energy $h\nu = hc/\lambda$, the absorbed photon flux $\phi_p(\lambda)d\lambda$ in the wavelength interval λ to $\lambda + d\lambda$ is given by

$$\phi_p(\lambda)d\lambda = \frac{2\pi\alpha c\lambda^{-4}[\exp(hc/\lambda kT_s)-1]^{-1}}{[\varepsilon_s(\lambda)]^{-1}+\{[R_c(\lambda)]^{-1}-1\}^{-1}}d\lambda \tag{8}$$

where α is the fraction of the converter area covered by active photovoltaic cells. These convert the absorbed photons into an electron flux $\phi_e(\lambda)d\lambda$ with a wavelength-dependent quantum efficiency $Q(\lambda)$.

$$\phi_e(\lambda)d\lambda = \phi_p(\lambda)Q(\lambda)d\lambda \tag{9}$$

Thus, the converter's short-circuit current density J_{sc} is given by

$$J_{sc} = e\int_0^\infty \phi_p(\lambda)Q(\lambda)d\lambda, \tag{10}$$

where e is the electronic charge.

Inserting Eqs. (8) and (9) into (10), the short-circuit current density J_{sc} is given by

$$J_{sc} = 2\pi\alpha c e \int_0^\infty \frac{\lambda^{-4} Q(\lambda)[\exp(hc/\lambda k T_s) - 1]^{-1}}{[\varepsilon_s(\lambda)]^{-1} + \{[R_c(\lambda)]^{-1} - 1\}^{-1}} d\lambda. \tag{11}$$

The open-circuit voltage V_{oc} of each photovoltaic cell is given by

$$V_{oc} = (kT_c/e)\ln[(J_{sc}/J_o) - 1], \tag{12}$$

where J_o is the saturation current density of the photovoltaic material. According to Boeing investigators, the value of J_o is given by

$$J_o = [2.555x10^{-4} T_c^3 \exp(-E_g/kT_c)] \text{ amps/cm}^2, \tag{13}$$

where the energy gap E_g for gallium antimonide is given by

$$E_g = [0.7 - 3.7x10^{-4}(T_c - 300^\circ K)] \text{ electron volts.} \tag{14}$$

The short-circuit current density J_{sc} and the open-circuit cell voltage V_{oc} can be used to compute the converter's maximum power output density

$$P_{max} = J_{sc} V_{oc} F, \tag{15}$$

where F is the fill factor, given by

$$F = \{1 - [\ln(J_{sc}/J_o)]^{-1}\}\{1 - \ln[\ln(J_{sc}/J_o)][\ln(J_{sc}/J_o)]^{-1}\}. \tag{16}$$

In designing the generator, we have assumed that at the maximum power point

$$J/J_{sc} = F^{1/3}, \tag{17}$$

$$V/V_{oc} = F^{2/3}, \tag{18}$$

which seems to be in good agreement with experimental data.

In applying the above series of equations, we require three sets of experimentally determined data: the heat source emissivity $\varepsilon_s(\lambda)$, the converter/filter reflectivity $R_c(\lambda)$, and the converter's quantum efficiency $Q(\lambda)$. The latter two sets were supplied to us by Boeing investigators (E. Horne, M. Morgan). As shown in Table 1, their data is given in terms of the wave number ω, the reciprocal of the wavelength λ. Therefore, it is convenient to recast Eq. (11) in terms of wave number:

6

$$J_{sc} = 2\pi\alpha c e \int_0^\infty \frac{\omega^2 Q(\omega)[\exp(hc\omega/kT_s)-1]^{-1}}{[\varepsilon_s(\omega)]^{-1} + \{[R_c(\omega)]^{-1}-1\}^{-1}}\,d\omega. \tag{19}$$

Two sets of data are listed in Table 1 for the filter's spectral reflectivity $R_c(\omega)$ and the cell's quantum efficiency $Q(\omega)$. For each property, the more conservative measured data set (M) is based on measurements of already fabricated non-optimized samples made by Boeing investigators for other applications, and the "improved" or "projected" data set (P) is based on their estimates of what improvements could be achieved by known stratagems for optimizing the filter and the photovoltaic cells for the present RTPV application. The illustrative example described in this section is based on the improved properties set, but later sections that summarize the results of our integrated RTPV system studies present results for both the more conservative measured performance parameters and the predicted improved properties. Our studies showed that the projected improvements in quantum efficiency had only a minor effect on system performance, but that the improved filter characteristics had a pronounced effect.

Table 1 Spectral Transmittance of Filter (AuC-2) and Quantum Eficiency of PV Cell (GaSb)

$\omega = 1/\lambda$

M = Measured
P = Projected

ω (cm⁻¹)	1-R_c(ω) M	1-R_c(ω) P	Q(ω) M	Q(ω) P
100	0.03	0.02	0.00	0.00
200	0.03	0.02	0.00	0.00
300	0.03	0.02	0.00	0.00
400	0.03	0.02	0.00	0.00
500	0.03	0.02	0.00	0.00
600	0.03	0.02	0.00	0.00
700	0.03	0.02	0.00	0.00
800	0.03	0.02	0.00	0.00
900	0.03	0.02	0.00	0.00
1000	0.03	0.02	0.00	0.00
1100	0.03	0.02	0.00	0.00
1200	0.03	0.02	0.00	0.00
1300	0.03	0.02	0.00	0.00
1400	0.03	0.02	0.00	0.00
1500	0.03	0.02	0.00	0.00
1600	0.03	0.02	0.00	0.00
1700	0.03	0.02	0.00	0.00
1800	0.03	0.02	0.00	0.00
1900	0.03	0.02	0.00	0.00
2000	0.03	0.02	0.00	0.00
2100	0.035	0.02	0.00	0.00
2200	0.035	0.02	0.00	0.00
2300	0.035	0.02	0.00	0.00
2400	0.035	0.02	0.00	0.00
2500	0.035	0.02	0.00	0.00
2600	0.035	0.03	0.00	0.00
2700	0.035	0.02	0.00	0.00
2800	0.035	0.02	0.00	0.00
2900	0.04	0.02	0.00	0.00
3000	0.04	0.02	0.00	0.00
3100	0.04	0.02	0.00	0.00
3200	0.04	0.02	0.00	0.00
3300	0.04	0.02	0.00	0.00
3400	0.05	0.02	0.00	0.00
3500	0.05	0.02	0.00	0.00
3600	0.05	0.02	0.00	0.00
3700	0.055	0.02	0.00	0.00
3800	0.055	0.02	0.00	0.00
3900	0.055	0.02	0.00	0.00
4000	0.06	0.02	0.00	0.00
4100	0.06	0.02	0.00	0.00
4200	0.065	0.02	0.00	0.00
4300	0.077	0.02	0.00	0.00
4400	0.08	0.02	0.00	0.00
4500	0.086	0.02	0.00	0.00
4600	0.097	0.02	0.00	0.00
4700	0.1	0.02	0.00	0.00
4800	0.112	0.02	0.00	0.00
4900	0.13	0.02	0.00	0.00
5000	0.14	0.03	0.00	0.00
5100	0.15	0.03	0.00	0.00
5200	0.17	0.03	0.00	0.00
5300	0.163	0.04	0.00	0.00
5400	0.205	0.055	0.00	0.00
5500	0.23	0.08	0.10	0.11
5600	0.255	0.11	0.24	0.26
5700	0.3	0.14	0.45	0.49
5800	0.325	0.16	0.55	0.60
5900	0.368	0.21	0.65	0.71
6000	0.377	0.25	0.67	0.73
6100	0.411	0.3	0.71	0.78
6200	0.45	0.34	0.73	0.79
6300	0.47	0.4	0.74	0.81
6400	0.49	0.47	0.75	0.82
6500	0.51	0.53	0.76	0.83
6600	0.523	0.6	0.77	0.84
6700	0.532	0.665	0.78	0.85
6800	0.54	0.725	0.78	0.85
6900	0.543	0.81	0.79	0.86
7000	0.54	0.83	0.79	0.85
7100	0.534	0.85	0.80	0.86
7200	0.528	0.84	0.80	0.86
7300	0.51	0.836	0.81	0.87
7400	0.49	0.795	0.81	0.87
7500	0.47	0.745	0.81	0.87
7600	0.443	0.695	0.81	0.87
7700	0.42	0.64	0.82	0.86
7800	0.39	0.56	0.82	0.86
7900	0.365	0.48	0.82	0.85
8000	0.34	0.41	0.82	0.85
8100	0.308	0.375	0.82	0.85
8200	0.28	0.35	0.82	0.85
8300	0.25	0.32	0.83	0.85
8400	0.23	0.29	0.83	0.84
8500	0.208	0.275	0.83	0.84
8600	0.19	0.26	0.83	0.83
8700	0.176	0.25	0.83	0.83
8800	0.155	0.24	0.82	0.83
8900	0.14	0.235	0.82	0.82
9000	0.13	0.23	0.82	0.81
9100	0.118	0.225	0.82	0.81
9200	0.1	0.225	0.82	0.80
9300	0.092	0.22	0.82	0.80
9400	0.08	0.22	0.82	0.78
9500	0.07	0.215	0.82	0.77
9600	0.06	0.21	0.81	0.76
9700	0.055	0.205	0.80	0.75
9800	0.05	0.2	0.80	0.74
9900	0.04	0.2	0.79	0.73
10000	0.035	0.195	0.78	0.71
10100	0.03	0.1875	0.77	0.70
10200	0.025	0.18	0.76	0.69
10300	0.023	0.1766	0.75	0.69
10400	0.021	0.1733	0.75	0.69
10500	0.02	0.17	0.74	0.68
10600	0.02	0.1666	0.73	0.67
10700	0.017	0.1633	0.72	0.66
10800	0.016	0.16	0.71	0.65
10900	0.02	0.157	0.70	0.64
11000	0.02	0.156	0.70	0.64
11100	0.025	0.155	0.69	0.63
11200	0.03	0.15	0.68	0.62
11300	0.035	0.15	0.67	0.61
11400	0.04	0.1	0.66	0.60
11500	0.05	0.1	0.65	0.59
11600	0.052	0.1	0.64	0.58
11700	0.053	0.1	0.63	0.58
11800	0.055	0.1	0.62	0.57
11900	0.056	0.1	0.61	0.56
12000	0.057	0.1	0.60	0.55
12300	0.055	0.1	0.60	0.55
12600	0.05	0.1	0.58	0.53
12900	0.045	0.1	0.56	0.51
13200	0.04	0.1	0.54	0.49
13500	0.04	0.1	0.52	0.49
13800	0.035	0.1	0.50	0.48
14100	0.03	0.1	0.48	0.47
14400	0.05	0.1	0.46	0.46
14700	0.05	0.1	0.45	0.46
15000	0.05	0.1	0.44	0.46
15300	0.05	0.1	0.43	0.46
15600	0.05	0.1	0.42	0.46
15900	0.05	0.1	0.40	0.45
16200	0.05	0.1	0.38	0.45
16500	0.05	0.1	0.36	0.44
16800	0.05	0.1	0.34	0.43
17100	0.05	0.1	0.32	0.42
17400	0.05	0.1	0.31	0.38
17700	0.05	0.1	0.30	0.37
18000	0.05	0.1	0.30	0.37
18300	0.05	0.1	0.30	0.37
18600	0.05	0.1	0.30	0.37
18900	0.05	0.1	0.32	0.40
19200	0.05	0.1	0.35	0.43
19500	0.05	0.1	0.38	0.47
19800	0.05	0.1	0.40	0.50
20100	0.05	0.1	0.41	0.43
20400	0.05	0.1	0.42	0.44
20700	0.05	0.1	0.43	0.45
21000	0.05	0.1	0.44	0.46
21300	0.05	0.1	0.45	0.47
21600	0.05	0.1	0.46	0.48
21900	0.05	0.1	0.47	0.49
22200	0.05	0.1	0.48	0.50
22500	0.05	0.1	0.50	0.53
22800	0.05	0.1	0.50	0.53
23100	0.05	0.1	0.50	0.53
23400	0.05	0.1	0.48	0.50
23700	0.05	0.1	0.45	0.48
24000	0.06	0.1	0.43	0.45
24300	0.05	0.1	0.40	0.42
24600	0.05	0.1	0.36	0.38
24900	0.05	0.1	0.36	0.38

ILLUSTRATIVE EXAMPLE

To illustrate the application of the above-derived equations, consider a heat source enclosed in a smooth tungsten-coated canister with the handbook-given [10] values of spectral emissivity $\varepsilon(\lambda)$ depicted by the solid curve of Figure 2. The canister operates at an illustrative temperature T_s = 1150°C = 1423°K, and radiates to a spectral filter and gallium antimonide photovoltaic cells at a converter temperature of T_c=0°C=273°K with an active area fraction α = 0.90.

Fig. 2 Spectral Emissivity of Tungsten Canister
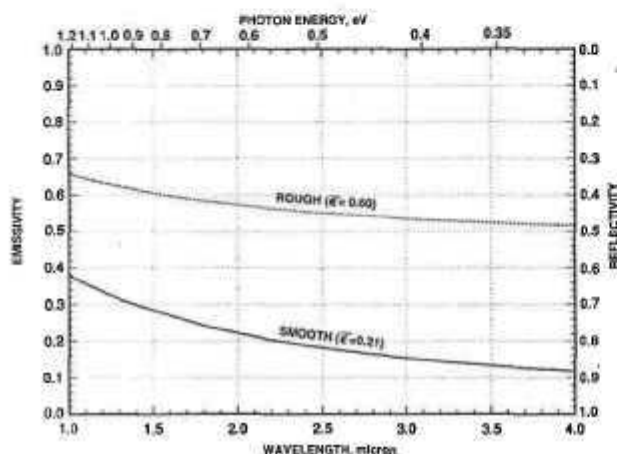
Fig. 3 Emission of Black Body and of Tungsten Canister (1150°C) and Absorption of Filtered Converter (0°C)
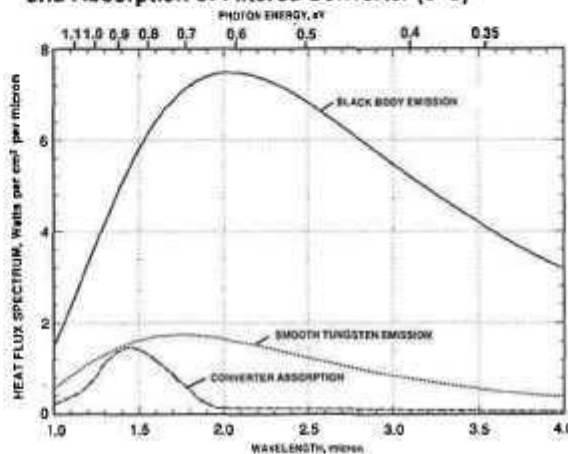
For the above temperatures, Figure 3 shows the spectral variation of the black-body radiation rate (Eq. 1), the radiative heat flux emitted by the smooth tungsten heat source canister (Eq. 2), and the net heat flux radiated from the canister to the filtered converter (Eq. 7). The difference between the tungsten emission curve and the converter absorption curve represents the effect of the spectral filter. As can be seen, at higher wavelengths most of the emitted radiation is reflected back to the heat source by the filter.

Figure 4 shows the photon flux absorbed by the filtered converter (Eq. 8), and the corresponding electron flux generated in the photovoltaic cells (Eq. 9). At each wavelength, the ratio of electron flux to photon flux represents the quantum efficiency of the gallium antimonide cells. As can be seen, at the shorter wavelengths or higher photon energies, the two curves are close together, indicating high quantum efficiencies. But at the higher wavelengths the two curves diverge, indicating poor quantum efficiencies of the GaSb cell, i.e., poor ability to convert absorbed protons into electrons. That is why the filter which reflects those wavelengths before they reach the PV cells is so beneficial to the converter's efficiency.

Fig. 4 Illustrative Example: Absorbed Photon Flux and Generated Electron Flux Spectra

8
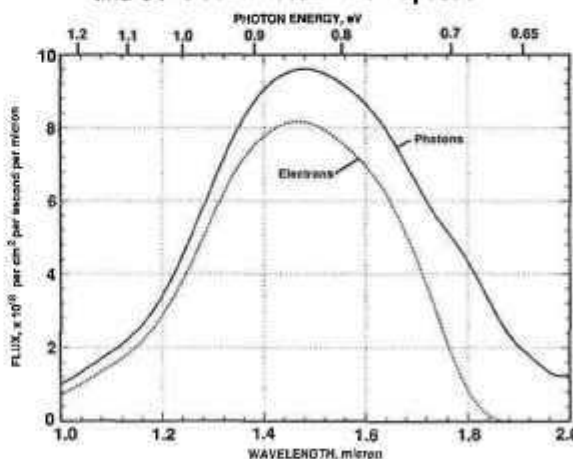
Applying numerical integration over the range of wavelengths to the illustrative example:

Eq. (9) gives the net heat flux absorbed by the converter q_{net} = 0.99 watt/cm^2,

Eq. (11) gives the short-circuit current density J_{sc} = 0.62 amp/cm^2,

Eqs. (12, 13, 14) give the open-circuit voltage V_{oc} = 0.50 volt,

Eq. (16) gives the fill factor F = 0.82,

Eq. (15) gives the maximum power density of the converter P_{max} = 0.25 watt/cm^2,

Eqs. (17) and (18) give the current density J = 0.58 amp/cm^2 and cell voltage V = 0.44 volt,

and the corresponding converter efficiency is $\eta = P_{max}/q_{net}$ = 25.2%.

Similar numerical integrations were carried out for a range of heat source temperatures T_s and converter temperatures T_c, with the parametric results displayed in Figures 5 through 8. Figure 5 shows that the net heat flux is only a function of the source temperature, and is essentially independent of the cell temperature in the range of interest.

Figures 6 and 7 show that the output power density and the converter efficiency are sensitive functions of the cell temperature. Lowering that temperature leads to significant performance improvements, albeit at the cost of increased radiator mass. Trade-offs between those parameters to maximize the system's specific power are described in a later section.

Fig. 5 Effect of Source Temperature on Net Heat Flux Absorbed by Converter
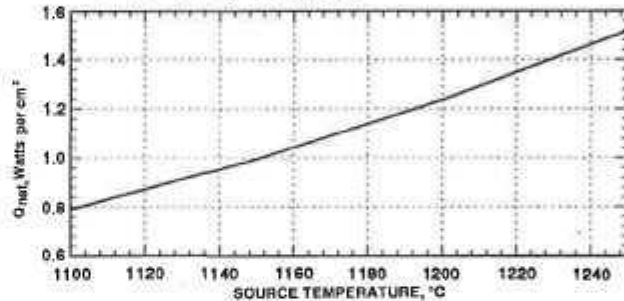
Fig. 6 Effect of Source and Cell Temperatures on Maximum Output Power Density of Converter
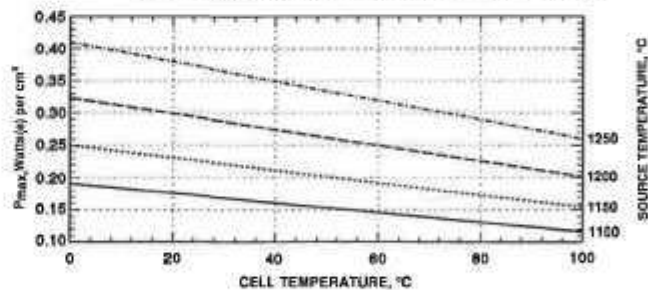
Fig. 7 Effect of Source and Cell Temperatures on Efficiency of Converter
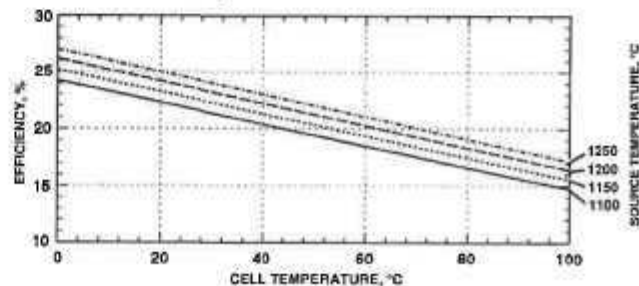
The results of Figures 5, 6, and 7 are combined in Figure 8, which presents cross-plots showing the effect of q_{net} on T_s, P_{max}, and η, for a range of cell temperatures T_c. It again shows the performance improvement obtainable by lowering the cell temperature.

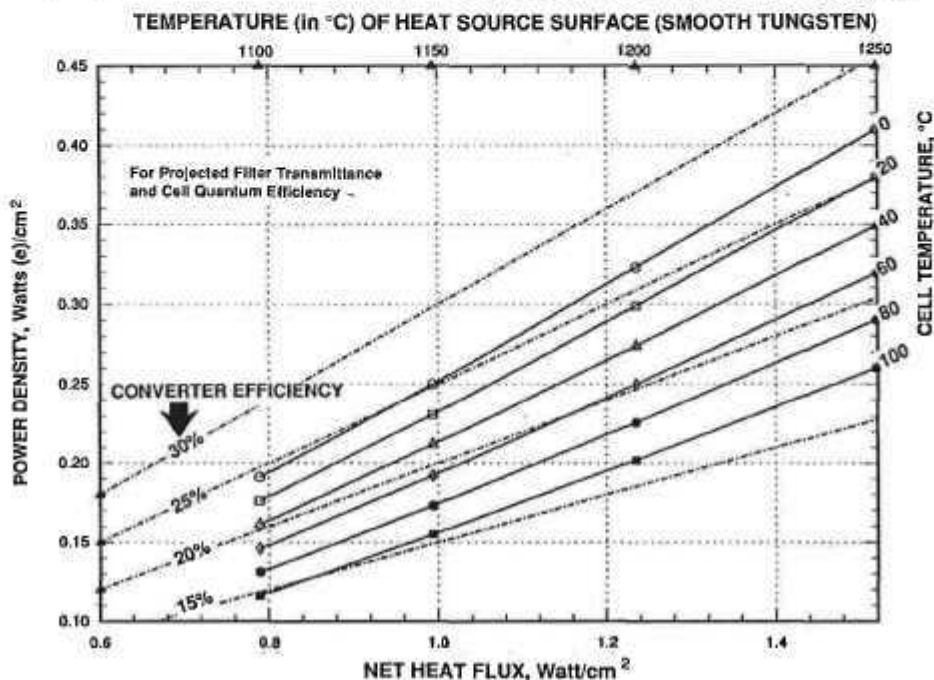Fig. 8 Effect of Net Heat Flux and Cell Temperature on Source Temperature, Power Density, and Efficiency

TEMPERATURE (in °C) OF HEAT SOURCE SURFACE (SMOOTH TUNGSTEN)

Figure 8 also shows that, for a given heat flux, higher source temperatures lead to higher power densities and efficiencies. From that, one might infer that these parameters can be significantly increased by lowering the heat source emissivity, which raises the source temperature for a given heat flux. But quite the opposite was found to be the case. This was discovered in the Fairchild study when the effect of roughening the tungsten surface on the converter's performance was analyzed.

The effective total emissivity, $\overline{\varepsilon}_s$, of the heat source canister is obtained by a weighted average of its spectral emissivity $\varepsilon_s(\lambda)$:

$$\overline{\varepsilon}_s = \frac{\int\limits_o^\infty \lambda^{-5}[\exp(hc/\lambda kT_s)-1]^{-1}\varepsilon_s(\lambda)d\lambda}{\int\limits_o^\infty \lambda^{-5}[\exp(hc/\lambda kT_s)-1]^{-1}d\lambda} \tag{20}$$

Applying the spectral emissivities for smooth tungsten shown by the solid curve in Figure 2 gives a value of 0.21 for $\overline{\varepsilon}_s$. It was assumed that roughening the tungsten (e.g., by grit blasting) would raise its effective total emissivity to 0.60. This corresponds to a 45% reduction of the smooth-tungsten spectral reflectivity $[1-\varepsilon_s(\lambda)]$, resulting in the spectral emissivity for roughened tungsten shown by the dashed curve of Figure 2.

10

The effect of that emissivity increase is shown in Figure 9, which compares the converter's computed performance for smooth and roughened canisters at a 0°C cell temperature. As can be seen, for the same heat flux the roughened canister actually yields a somewhat higher power density and converter efficiency, contrary to expectations. And it does so at an appreciably lower heat source temperature (by almost 100°C). Since lowering the heat source temperature without loss of performance is a desirable goal, our RTPV design study assumed the use of a roughened tungsten canister.

Fig. 9 Effect of Canister Roughness on its Temperature, Converter Efficiency, and Output Power
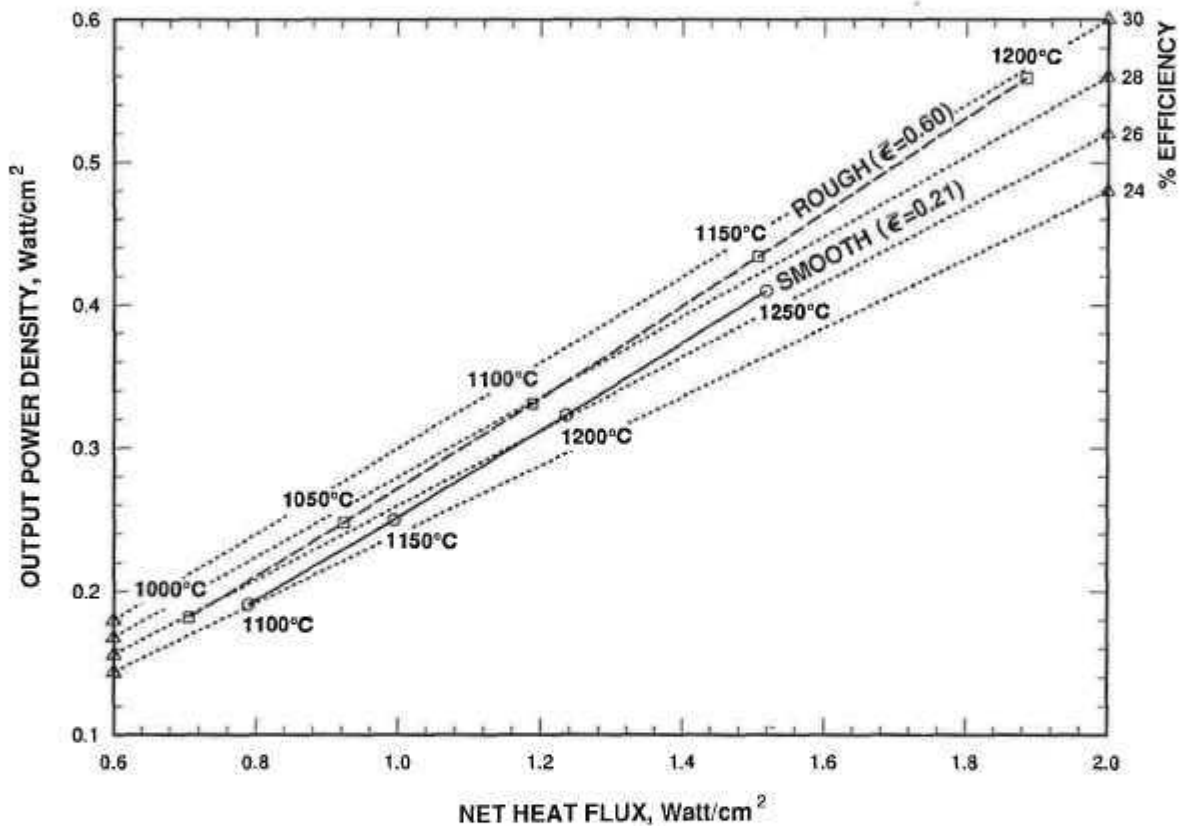
SYSTEM DESIGN

This section presents a description of the radioisotope heat source, the TPV converter, and the heat rejection radiator, and their system integration. Thermal, electrical, and structural analyses and optimization of the integrated system are presented in subsequent sections.

The radioisotope heat source for the RTPV design, like that for the RTG options analyzed in Fairchild's PFF study last year [7], are based on the General Purpose Heat Source (GPHS) modules [11]. These are the same modules that were used in the RTGs flown on the Galileo and Ulysses missions after very extensive safety analyses and tests and after passing stringent safety reviews, and that are slated for launch on the upcoming Cassini mission.

11

As shown in Figure 10, each GPHS module has a maximum thermal power of 250 watts, and contains four $^{238}PuO_2$ fuel pellets encapsulated in iridium-alloy clads designed to contain or immobilize the fuel in case of accidents before, during, and after launch. The remaining module components are graphitic and are designed to protect the integrity of the iridium clads. There are two impact shells and one aeroshell made of fine-weave pierced fabric (FWPF), a very tough high-temperature three-dimensional carbon-carbon composite.

Fig. 10 GPHS–General -Purpose Heat Source Module (250 Watts) Sectioned at Mid-Plane

AEROSHELL (FWPF*)
THERMAL INSULATION (CBCF**)
IMPACT SHELL (FWPF*)
CLAD (Ir)
FUEL***

9.72 cm

2.65 cm

9.32 cm
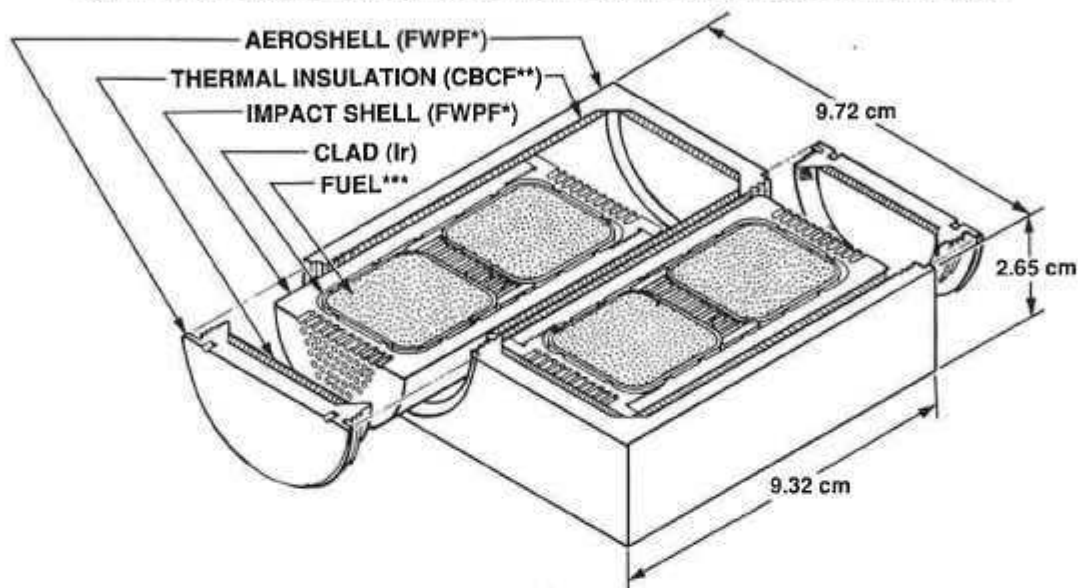
*Fine-Weave Pierced Fabric, a 90%-dense 3D carbon-carbon composite
**Carbon-Bonded Carbon Fibers, a 10%-dense high-temperature insulator
***62.5-watt $^{238}PuO_2$ pellet

The impact shells help to prevent breach of the clads during impact, and the aeroshell serves as an ablator in case of inadvertent atmospheric reentry. Between the impact shells and the aeroshell is a high-temperature thermal insulator consisting of a low-density composite of carbon-bonded carbon fibers (CBCF), to prevent overheating of the clads during the reentry heat pulse and overcooling and embrittlement of the clads during the subsequent subsonic atmospheric descent before earth impact.

For the present study, it was decided to base the RTPV generator design on the use of two GPHS modules, which is a 60% reduction from the five modules used in the RTG design for PFF [8]. Figures 11 and 12 display vertical and horizontal cross-sections of the two-module heat source and of the photovoltaic converter, and Figure 15 shows an exploded trimetric view. The dimensions shown are in inches. As can be seen, the heat source's graphitic aeroshell is enclosed in an approximately cubical molybdenum canister. The inside of the canister's end caps is lined with iridium to prevent contact between the graphite and molybdenum. The outside of the canister's side walls is coated with tungsten to minimize sublimation, and also because tungsten has more favorable spectral emissivity characteristics than molybdenum. Both the inside and outside of the canister's side walls are roughened to raise their effective total emissivity to 0.60.

As seen in Figure 11, the canister has a vent tube to release the helium formed by alpha decay of the Pu-238 fuel to space. The vent tube terminates in a semi-permeable Viton seal, designed to maintain an internal pressure of a fraction of an atmosphere at the helium generation rate of 654 scc per year from the 500 watt(t) heat source. This pressure range is low enough to prevent excessive stress in the canister, but high enough to provide continuum conduction in the internal gas gaps, which greatly reduces the clad temperature. Reduced clad temperatures reduce grain growth and consequent embrittlement of the iridium alloy which is of critical importance in case of subsequent inadvertent Earth impact.

Fig. 11 Vertical Cross-Section of Converter
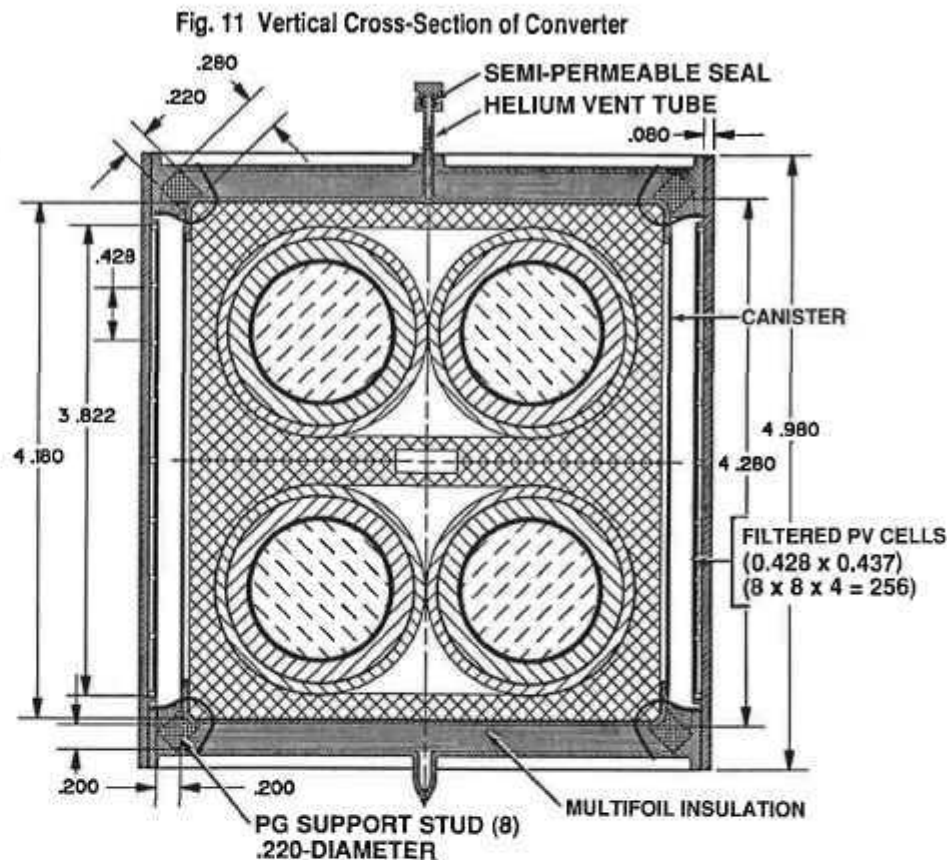
Since the heat source modules are contained in a monolithic canister, unlike the stack of unsupported modules used in preceding RTGs [12], there is no need for a complex axial preload mechanism to hold the stack together during launch vibration. As indicated in Figure 11, each of the canister's eight corners is supported by a small cylindrical pyrolitic-graphite (PG) stud. PG has good compressive strength, and the axes of the eight cylindrical support studs all point at the center of the heat source. Thus, shear loads are minimized, and the canister is supported in every direction by compressive loads on the PG studs.

The thermal conductivity of PG is highly anisotropic, being two orders of magnitude lower in the c-direction than in the a-direction. The cylindrical studs are machined so that their axes lie in the c-direction to minimize thermal losses. For the dimensions shown, our analysis showed that only 3.6% of the heat source's thermal power is lost through the support studs.

As shown in Figure 11, the canister's two end faces are thermally insulated by a multifoil assembly, identical to those used in previous thermoelectric converters, and consisting of 60 layers of 0.0003" Mo foils separated by ZrO_2 spacer particles. Our analysis showed that only 2.2% of the thermal power is lost through the multifoil insulation. Thus, 94.2% of the generated heat is absorbed by the converter.

13

As indicated in Figures 11 and 12, each of the canister's four side faces radiates heat to a photovoltaic array of 8 x 8 gallium antimonide cells covered by a spectral filter. Each rectangular cell has dimensions of 0.428" x 0.437" (1.09 cm x 1.11 cm). At each horizontal level, the cells are parallel-connected in groups of four, and these groups of parallel cells are series-connected in the converter's corners to groups in the next horizontal level. Thus, each generator side has two series-parallel networks of 8x4 cells, and the generator's eight networks are connected in series with each other. The series connectors are not shown but they could be formed by spot-welding projecting tabs located in the four empty housing corners shown in Figure 12.

Fig. 12 Horizontal Cross-Section of Converter
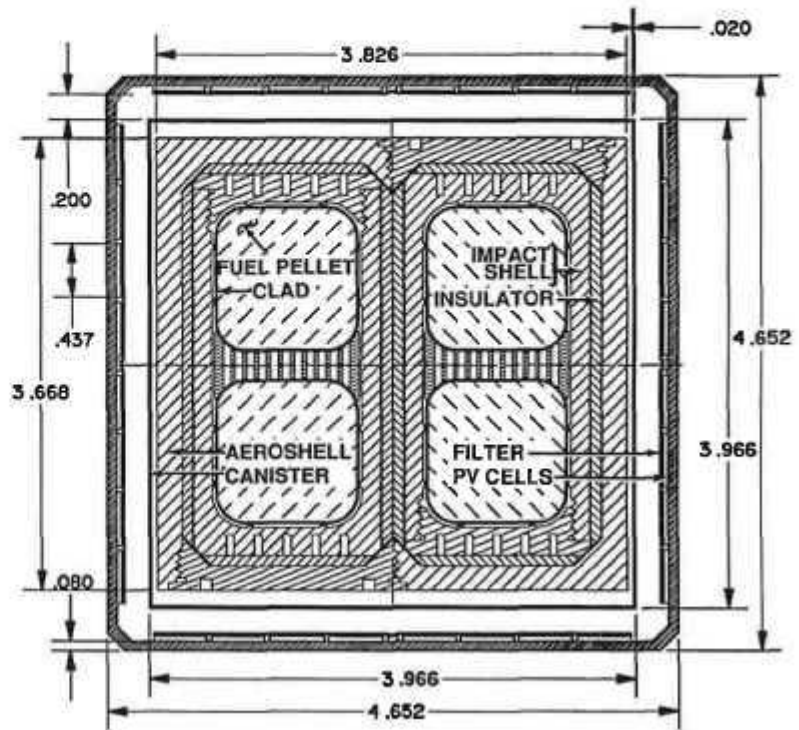
A schematic view of the cell interconnections is shown in Figure 13 for one generator side and in Figure 14 for all four sides. As seen, each side has terminals at its lower corners. At three corners of the generator the terminals of neighboring sides are connected together to form a 64x4 series-parallel network. At the fourth corner, leads from the two terminals are brought out of the generator housing through insulated feedthroughs. For the 0.44V cell voltage shown in the previously discussed illustrative example, the total generator would have an output of about 28 volts.

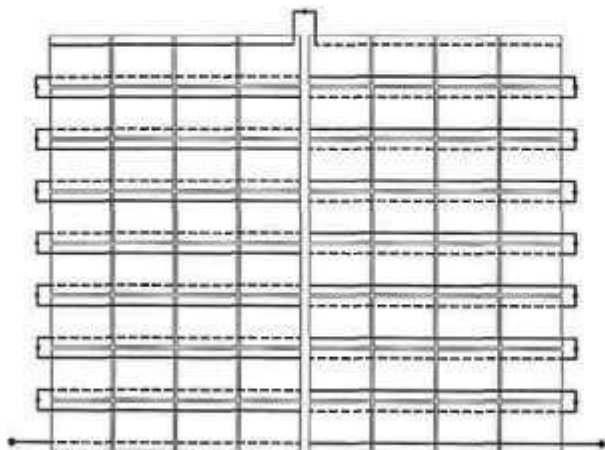Fig. 13 Schematic View of Series-Parallel Network Connecting the 64 PV Cells on Each Converter Face
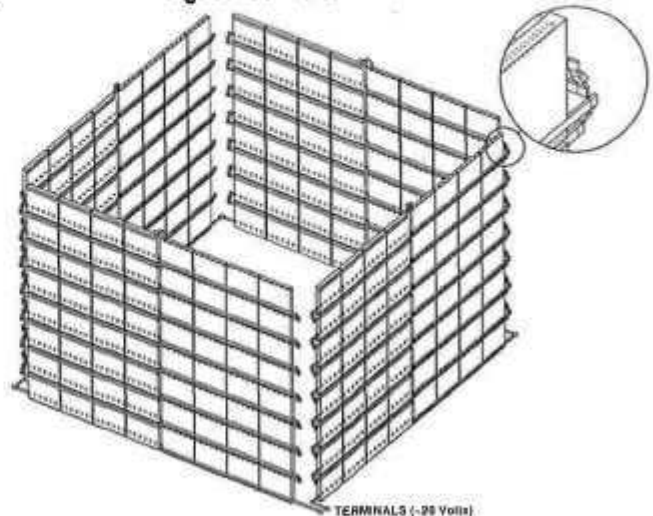
Fig. 14 Converter Network

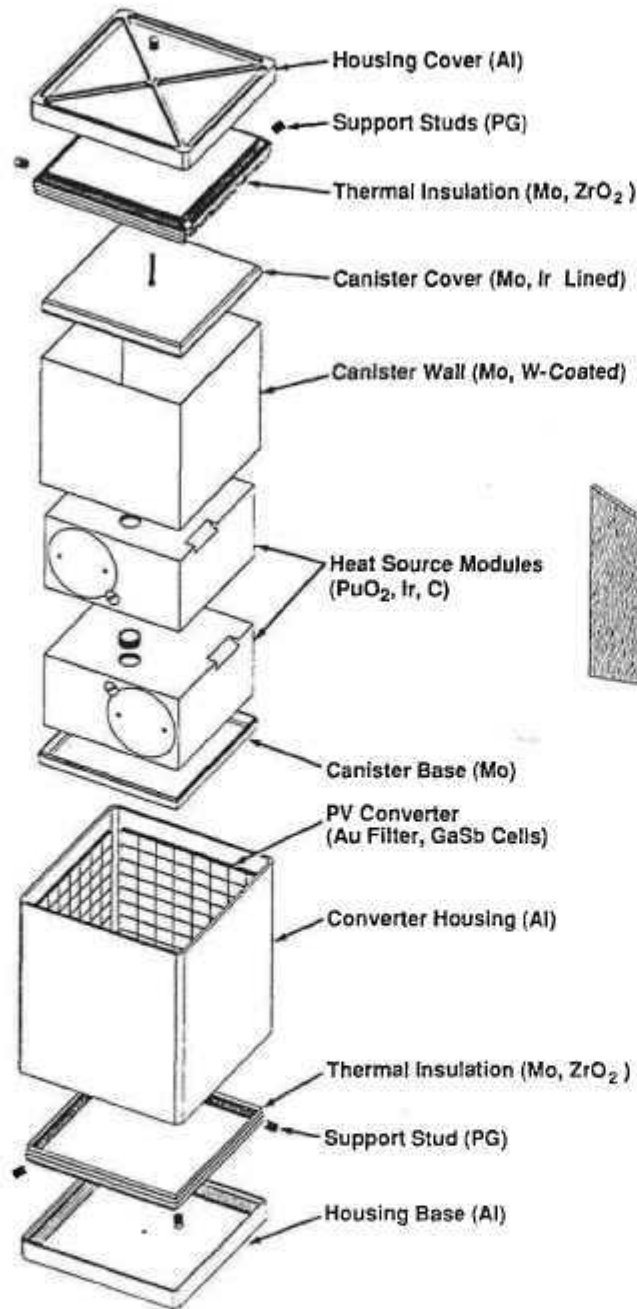14

Fig. 15 Exploded View of Converter

- Housing Cover (Al)
- Support Studs (PG)
- Thermal Insulation (Mo, ZrO_2)
- Canister Cover (Mo, Ir Lined)
- Canister Wall (Mo, W-Coated)
- Heat Source Modules (PuO_2, Ir, C)
- Canister Base (Mo)
- PV Converter (Au Filter, GaSb Cells)
- Converter Housing (Al)
- Thermal Insulation (Mo, ZrO_2)
- Support Stud (PG)
- Housing Base (Al)

Fig. 16 RTPV Generator Overview
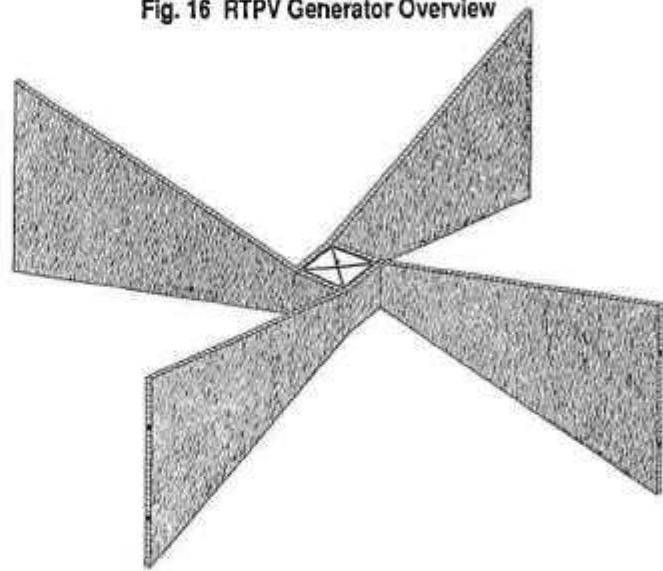
Figure 15 depicts an exploded view of the heat source and the converter, and Figures 16 and 17 present an assembled and an exploded view of their integration with the heat rejection system.   As shown, there is a large trapezoidal radiator fin bonded to each side face of the converter housing. The RTPV needs much larger radiator fins than typical RTGs, because they must operate at much lower heat rejection temperatures to achieve their high efficiencies. The optimum dimensions, i.e., the dimensions that maximize the system's specific power, were determined by detailed analyses described later. Detailed analyses are warranted because the radiators are the biggest mass component of the RTPV system.

15

Fig. 17 Exploded View of RTPV Generator and of Radiator Fin

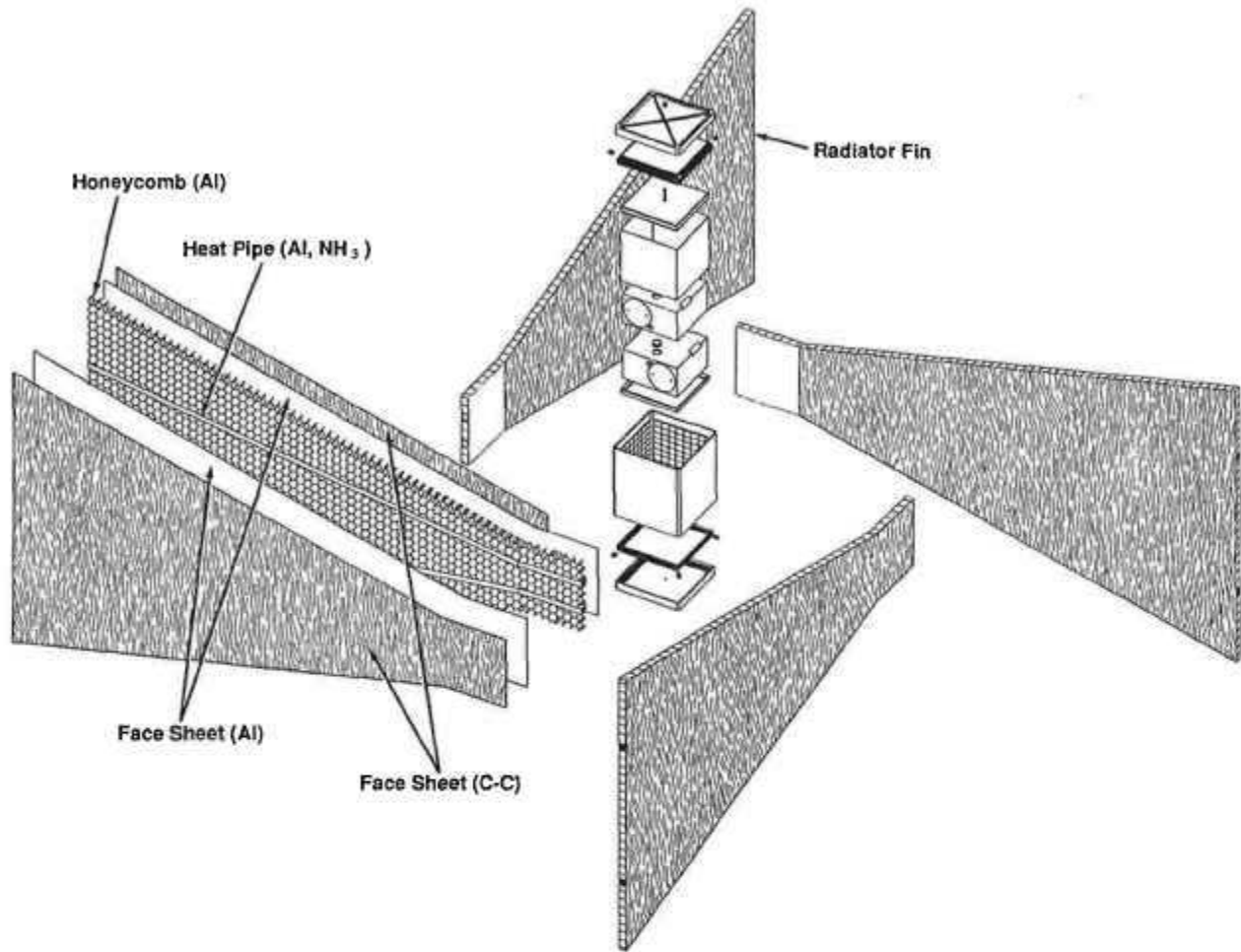Fig. 17 Exploded View of RTPV Generator and of Radiator Fin

Figure 17 shows an exploded view of the generator and of one of the four radiator fins. The exploded fin view shows a central core consisting of an aluminum honeycomb with two embedded Al/NH$_3$ heat pipes. To each face of the honeycomb core two skins are bonded: an inner skin of aluminum to provide structural strength for resisting bending moments during launch; and an outer skin consisting of a graphitized carbon-carbon composite to provide high thermal conductance in the fiber direction. As indicated by the shading, the graphite fibers are oriented in the vertical direction, normal to the heat pipes' axes. In that direction they have a thermal conductivity twice that of copper, at about one fourth its density [13]. They serve to distribute the heat from the heat pipes over the width of the fin. They also provide the fin with high-emissivity surfaces. In our structural analysis we assumed that the graphite skin contributes zero strength in the direction normal to the fibers.

STRUCTURAL ANALYSIS

To optimize the system design, particularly the fin design that maximizes the generator's specific power, we must first perform a static and dynamic structural analysis to ensure that the long fins required for the desired low cell temperatures can survive the predicted launch loads without excessive stresses in their aluminum skins.

Consider a fin of root-to-tip length x_1, honeycomb thickness z_o, and height y varying from y_o at the fin tip to y_1 at the fin root. Let x denote the horizontal distance from the fin tip. Then the fin height y at position x is given by

$$y = y_o - x(y_o - y_1)/x_1 = y_o - y'x, \tag{21}$$

where y' is defined as $(y_o - y_1)/x_1$.

The total mass dm of the fin segment between x and $x + dx$ is given by

$$dm = [2m_1 + m_2 y + 2m_3 y t_o]dx, \tag{22}$$

where m_1 is the mass per unit length of each heat pipe, m_2 is the mass per unit area of the honeycomb plus that of the two graphite skins and of the bond between them, m_3 is the volumetric density of the aluminum skins, and t_o is the thickness of each aluminum skin. Combining Eqs. (21) and (22), we obtain

$$dm = [2m_1 + (m_2 + 2m_3 t_o)(y_o - y'x)]dx. \tag{23}$$

When the fin is subjected to an acceleration load of magnitude g normal to its surface, the resultant bending moment M at position x is given by

$$M = g\int_o^x (x - x')[2m_1 + (m_2 + 2m_3 t_o)(y_o - y'x')]dx', \tag{24}$$

where x' is the variable of integration. Integrating Eq. (24) from $x'=0$ to $x'=x$, we obtain

$$M = g[m_1 x^2 + (m_2 + 2m_3 t_o)(\tfrac{1}{2} y_o x^2 - \tfrac{1}{6} y'x^3)]. \tag{25}$$

The maximum tensile stress σ in the aluminum fin at position x is given by

$$\sigma = (\tfrac{1}{2}z)M/I, \tag{26}$$

where I, the combined moment of inertia of the aluminum skins and the heat pipes at position x, is given by

$$I = \tfrac{1}{12}y[(z + 2t_o)^3 - z^3] + 2I_o, \tag{27}$$

and where I_o is the moment of inertia of each heat pipe. Assuming that each heat pipe has a rectangular cross-section of base width b, depth z, and wall thickness w, its moment of inertia is given by

$$I_o = \tfrac{1}{12}[bz^3 - (b - 2w)(z - 2w)^3]. \tag{28}$$

17

Since the aluminum skin thickness t_o is much smaller than the honeycomb thickness z, Eq. (28) reduces to

$$I = \tfrac{1}{2} y z^2 t_o + 2 I_o. \tag{29}$$

Inserting Eqs. (25) and (29) into (26), the maximum tensile stress σ at position x is given by

$$\sigma = \frac{g[(m_1 + \tfrac{1}{2} m_2 y_o + m_3 y_o t_o) x^2 - \tfrac{1}{6}(m_2 + 2 m_3 t_o) y' x^3]}{(y_o - y' x) z t_o + 4 I_o / z}. \tag{30}$$

As an illustrative example, consider a fin of length x_1=30", thickness z=0.5", fin tip height y_o=20", fin root height y_1=5.0", and graphite thickness of 0.005". (As will later be shown, the generator's specific power is maximized with very thin graphite skins.) Assume that the heat pipe mass m_1 per unit length is 1.61 g/cm; that the mass per unit area of the honeycomb is 0.063 g/cm^2, that of each 0.005" graphite skin is 0.025 g/cm^2; that of each bond layer is 0.022 g/cm^2, so that the areal density m_2 is 0.157 g/cm^2; that the volumetric density m_3 of the aluminum skins is 2.77 g/cm^3; and that the fin is subjected to quasi-static acceleration of 40 g or 392 m/s^2 normal to its surface. This last assumption was made because previous RTGs [14] were designed and qualification-tested to 40 g, but it is quite conservative for the present application, because the RTPV under study is much shorter than the RTGs, and because a quasi-static test may inherently be an overconservative representation of the dynamic launch loads.

For the above parameters, Figure 18 presents stress profiles computed from Eq. (30) for aluminum skin thicknesses t_o ranging from 0.003" to 0.010". As can be seen, decreasing the skin thickness increases the stress, but not very much because the effect of the smaller cross-sectional area is largely compensated by the reduced fin weight.

Let σ_o denote the maximum allowable tensile stress in the aluminum alloy. For a yield stress of 35 ksi, a safety factor of 1.5 gives an allowable stress of 23 ksi or 159 MPa. As can be seen, over most of the fin length the computed maximum stress displayed in Figure 18 is less than the allowable stress. Even for the thinnest aluminum skin (0.003") this is true for 24" of the 30" fin length. But near the fin root, the skin stress exceeds the allowable limit. To avoid this, the skin thickness must be gradually increased near the fin root.

In general, the maximum stress σ_1 at the fin root $(x=x_1)$ for a uniform skin thickness t_o is given by

$$\sigma_1 = \frac{g[(m_1 + \tfrac{1}{2} m_2 y_o + m_3 y_o t_o) x_1^2 - \tfrac{1}{6}(m_2 + 2 m_3 t_o) y' x_1^3]}{y_1 z t_o + 4 I_o / z}. \tag{31}$$

Fig. 18 Tensile Stress Profile Produced by 40-G Side Load on Fin with 20" Tip Height, 4.7" Base Height
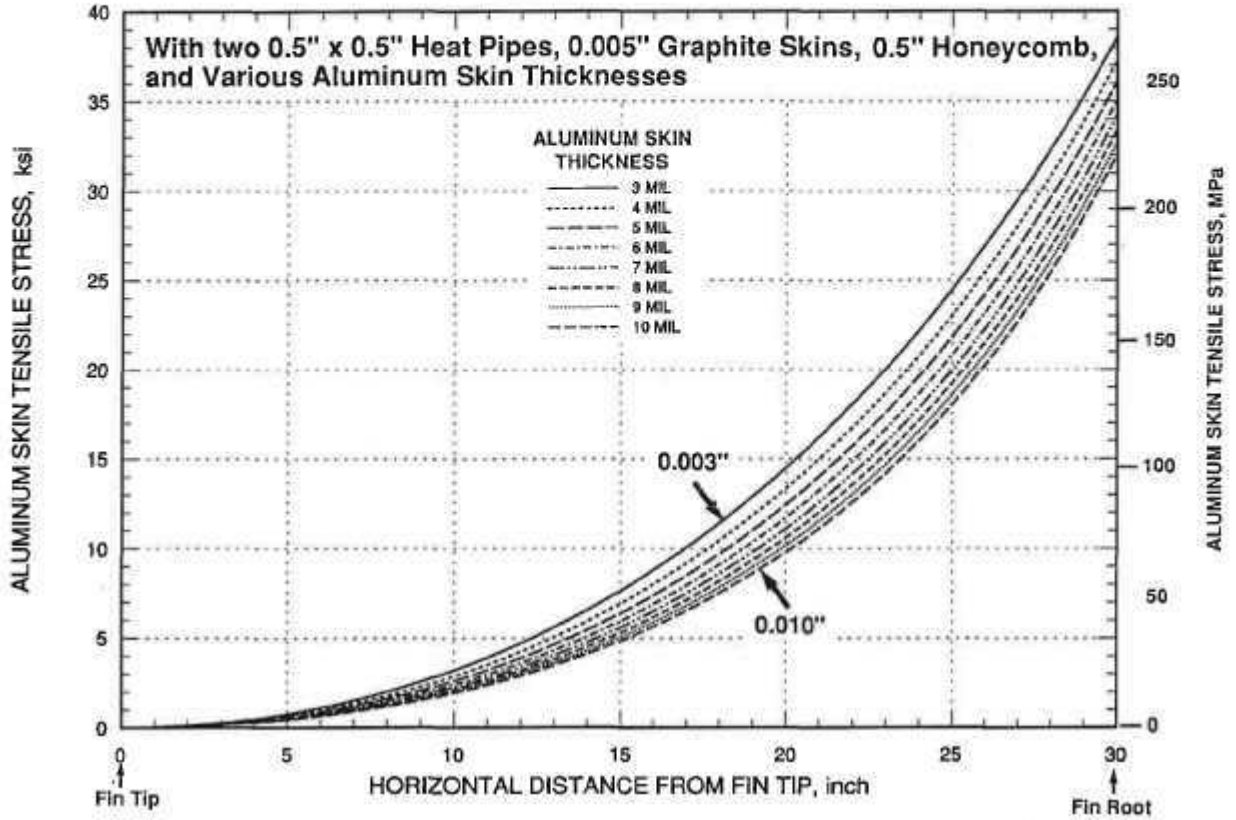
If $\sigma_l < \sigma_o$, the fin can use a uniform skin thickness t_o without exceeding the allowable stress limit σ_o. But if $\sigma_l > \sigma_o$, the skin thickness near the fin root must be increased to avoid excessive stress. For that case, the cross-over point x_o beyond which the assumed skin thickness t_o is inadequate can be obtained by setting σ equal to σ_o in Eq. (30) and solving the resultant cubic equation for x_o:

$$[\tfrac{1}{6}g(m_2 + 2m_3t_o)y']x_o^3 - [g(m_1 + \tfrac{1}{2}m_2y_o + m_3y_ot_o)]x_o^2 - [\sigma_oy'zt_o]x_o + \sigma_o[y_ozt_o + 4I_o/z] = 0 \quad (32)$$

For $x_o < x < x_1$, the skin thickness t must be increased above t_o to avoid excessive stress. The required value of t at position x is obtained from Eq. (30), by setting $\sigma = \sigma_o$ and solving for t_o in the denominator:

$$t = \frac{g[(m_1 + \tfrac{1}{2}m_2y_o + m_3y_ot_o)x^2 - (\tfrac{1}{6}m_2 + \tfrac{1}{3}m_3t_o)y'x^3]}{z\sigma_o(y_o - y'x)} - \frac{4I_o/z^2}{y_o - y'x}. \quad (33)$$

Note that Eq. (33) is not quite accurate, because it omits the additional moment due to the thickened skin near the fin root. But the error introduced by that omission was shown to be quite small, because where the skin is thickened the moment arm is short and the fin height is relatively small.

19

Since the stress profiles displayed in Figure 18 for the illustrative example exceed the allowable stress limit of 23 ksi at $x=x_1$, the aluminum skins near the fin root must be increased in accord with Eq. (33). This is illustrated in Figure 19 for a range of initial skin thicknesses ranging from 0.003" to 0.010", and in Figure 20 for fin lengths ranging from 20" to 40", honeycomb thicknesses of 0.38" and 0.50", and skin thicknesses of 3 to 6 mils.

Fig. 19 Required Aluminum Skin Thickness Profiles to Keep Tensile Stress Below 23 ksi
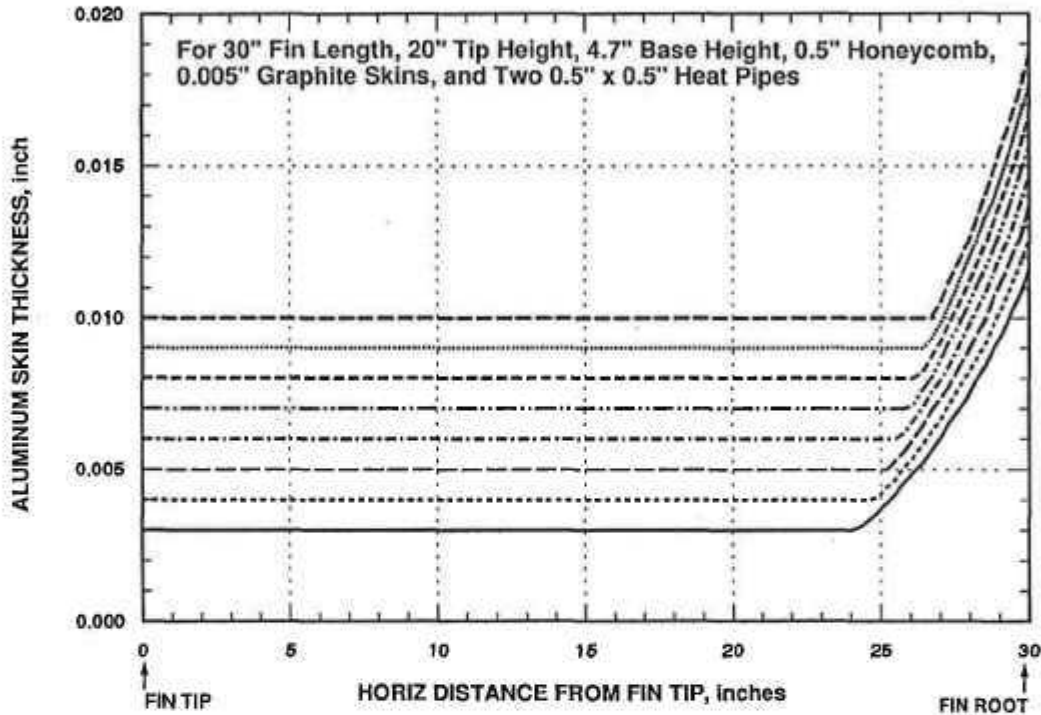
Fig. 20 Effect of Fin Length and Honeycomb Thickness on Required Aluminum Skin Thickness at Fin Root

20
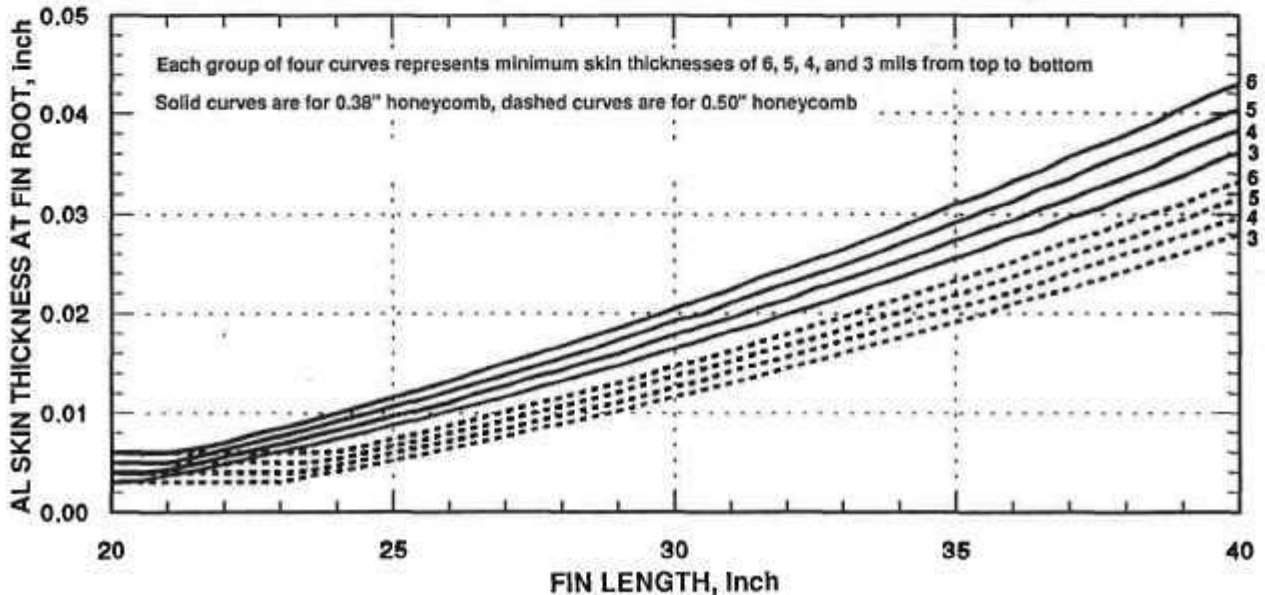
Figure 19 shows that reducing the initial skin thickness will lighten the radiator even when the required skin thickening near the fin root is taken into account. Therefore, in our design study the aluminum skin thickness, except near the fin root, was fixed at 0.003", which was deemed the minimum practical thickness.

Figure 20 shows that increasing the honeycomb thickness reduces the required skin thickness, as would be expected. However, the skin mass reduction must be traded off against the honeycomb mass increase. The mass m of the two aluminum skins on the fin segment projecting beyond the housing is given by

$$m = 2m_3 \int_0^{x_1} (y_o - y'x)t\,dx. \tag{34}$$

If $x_o > x_1$, the skin has a uniform thickness t_o, and its mass is given by

$$m = 2m_3 t_o [y_o x_1 - \tfrac{1}{2} y' x_1^2]. \tag{35}$$

If $x_o < x_1$, the skin thickness t between x_o and x_1 is increased, and the total skin mass m is given by

$$m = 2m_3 [t_o \int_0^{x_o} (y_o - y'x)\,dx + \int_{x_o}^{x_1} (y_o - y'x)t\,dx] \tag{36}$$

Combining Eqs (33) and (36), we obtain

$$m = 2m_3 t_o \int_0^{x_1} (y_o - y'x)\,dx$$

$$+ 2m_3 \int_{x_o}^{x_1} \{(g/z\sigma_o)[(m_1 + \tfrac{1}{2}m_2 y_o + m_3 y_o t_o)x^2 - (\tfrac{1}{6}m_2 + \tfrac{1}{3}m_3 t_o)y'x^3] - (4I_o/z^2)\}\,dx. \tag{37}$$

Finally, integration of Eq. (37) gives the aluminum skin mass per projecting fin:

$$m = 2m_3 \{t_o y_o x_o - \tfrac{1}{2}t_o y' x_o^2 - (4I_o/z^2)(x_1 - x_o)$$

$$+ (g/z\sigma_o)[\tfrac{1}{3}(m_1 + \tfrac{1}{2}m_2 y_o + m_3 y_o t_o)(x_1^3 - x_o^3) - \tfrac{1}{24}(m_2 + 2m_3 t_o)y'(x_1^4 - x_o^4)]\}. \tag{38}$$

From this, the total radiator mass for a given set of input parameters can be computed. This was done for fin lengths ranging from 20" to 40", for aluminum skin thicknesses (except near the fin roots) of 3, 4, 5, and 6 mils. The results for honeycomb thicknesses of 0.38" (solid curves) and 0.50" (dashed curves) are displayed in Figure 21, which shows the effect of fin length on the total radiator mass, including the thickened aluminum skins near the fin roots that are needed to avoid excessive stress.

21

Fig. 21 Effect of Fin Length and Honeycomb Thickness on Total Radiator Mass
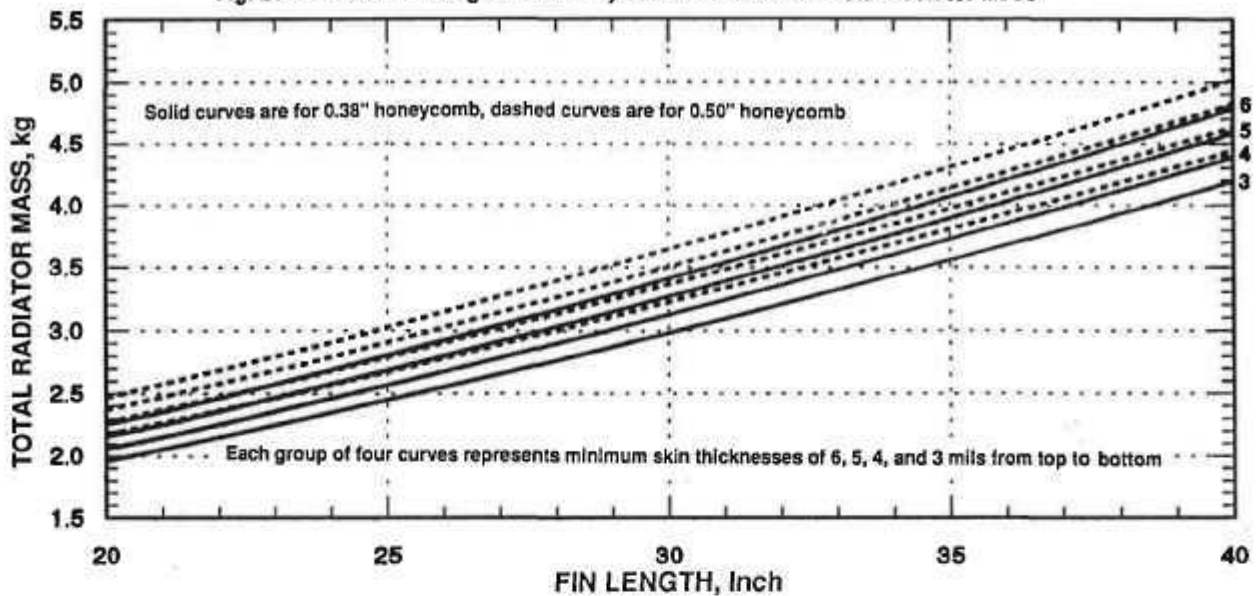
As was shown in Figure 20, increasing the honeycomb thickness reduces the required skin thickness. But Figure 21 shows that the resultant mass saving is less than the additional honeycomb mass. Consequently, the total radiator mass is somewhat lower for the 0.38" honeycomb than for the 0.50" thickness.

The preceding quasi-static analysis was supplemented by a dynamic analysis using a detailed NASTRAN [15] model of the radiator fin consisting of 966 nodes and 1717 elements. A plate element mesh was used for each of the two aluminum face sheets and for the two graphitized carbon-carbon sheets. The honeycomb core was modeled with four layers of solid elements, and the heat pipe walls were represented by a number of plate elements.

Since the graphitized carbon-carbon material is highly anisotropic, orthotropic material properties were used in the NASTRAN model. The modulus of elasticity in the vertical carbon fiber direction was assumed to be eight times larger than the modulus of elasticity in the fin length direction. The honeycomb core is also orthotropic and was assumed to have its higher shear strength L-direction (ribbon direction) oriented in the long fin direction, and its W-direction (transverse to the ribbon) parallel to the vertical axis.

Parametric studies were conducted on several fin configurations of interest. Each configuration was assessed by performing a modal analysis and using its results in a random analysis. The results were reassuring for the smaller fin sizes, but as the fin areas increased, so did concern about the possible acoustic response of the structure.

An acoustic analysis of one of the larger fin sizes (30" length by 20" tip height with a 0.5" honeycomb) was conducted using the VAPEPS (VibroAcoustic Payload Environment Prediction System) computer code [16]. VAPEPS is maintained and managed for NASA by JPL. In this analysis, four different qualification-level acoustic environments were used as input. They were the STS baseline 9' diameter payload, the STS maximum 15' diameter payload, the Titan III, and the Delta II vehicle with 10' fairing. The results of the four acoustic response analyses are plotted in Figure 22.

22

Fig. 22 Acoustic Response of 30" Radiator Fin for Various Launch Vehicles
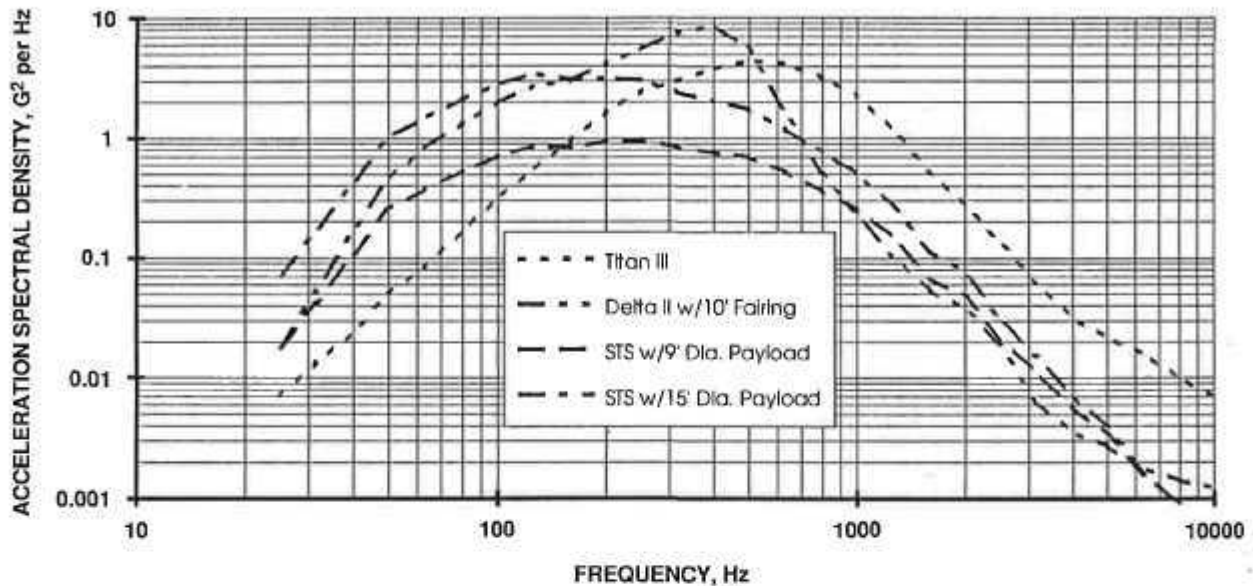
The above radiator configuration was analyzed for the acoustic response curve of the STS with a 9 ft diameter payload, since this is the most likely launch vehicle to be used for the Pluto Fast Flyby mission. (Another launch vehicle, the Russian Proton, is under active consideration, but an acoustic analysis of that option must await the availability of data similar to that used to generate Figure 22.) For the 11' STS option, an equivalent quasi-static pressure on the fin was calculated by summing the products of modal mass and dynamic force on a mode-by-mode basis. Stresses in the radiator fin due to the equivalent static pressure were then calculated. A 10-minute duration of the acoustic loading was assumed. An equivalent number of stress reversal cycles (184,378 cycles) for the radiator fin was derived from the modal participation data and the acoustic response curve. Finally, Miner's cumulative fatigue damage index [17] was calculated based on the S-N curves for 6061-T6 aluminum. The index sums the ratios of 1-, 2-, and 3-sigma stress reversal cycles to their corresponding allowable fatigue curve cycles. The results indicated that for the postulated launch vehicle, the 30"-long fin will satisfy Miner's fatigue requirement with ample margin (M.S. = +0.69).

SYSTEM ANALYSIS AND OPTIMIZATION

Determining the optimum system design, particularly the fin design that maximizes the system's specific power, requires a coupled thermal and electrical analysis. In that analysis, the heat generation rate is known, but the heat source surface temperature T_s and cell temperature T_c are not. Therefore, the analysis must be carried out iteratively. The coupled analysis was carried out by means of a thermal analysis code, SINDA [18], that had been modified by Fairchild, and by a standard thermal radiation code, SSPTA [19]. For the former we constructed a 197-node model, and for the latter a model consisting of 496 surfaces.

23

Fairchild made two major modifications in the thermal analysis code. The net heat flux q_{net} from the sides of the heat source to the converter cells at each iteration was computed by integration of Eq. (7),

$$q_{net} = 2\pi hc^2 \int_0^\infty \frac{\lambda^{-5}[\exp(hc/\lambda kT_s)-1]^{-1}}{[\varepsilon_s(\lambda)]^{-1}+\{[R_c(\lambda)]^{-1}-1\}^{-1}} d\lambda, \qquad (39)$$

with appropriate corrections for gaps between cells and obstruction by the electrical grid; and the waste heat flowing to the radiator fins was computed by subtracting the converter's electrical power generation rate from the heat generation rate of the heat source. The power generation rate was computed by multiplying the total cell area of the generator by the power density P_{max} obtained from Eqs. (11) through (16). The two thermal codes computed a new set of canister and cell temperatures, which were used as inputs in the next iteration. This iterative procedure was repeated until the modified code converged on a consistent solution.

Let us first examine the effect of varying the graphite skin thickness on system characteristics for a set of illustrative parameters. For a 30" root-to-tip fin length, a 20" tip height, a 0.38" honeycomb thickness, a 0.003" aluminum skin thickness, and a converter with 90% active cell area, the effect of varying the graphite skin thickness from 0 to 0.030" is illustrated in Figure 22. The figure shows the effect of graphite skin thickness on system mass, cell temperature, output power, system efficiency, and specific power. In each of the three figures, the solid curve represents results based on measured values of filter transmittance and cell quantum efficiency, and the dashed curve is based on projected values as listed in Table I.

Fig. 23 Effect of Graphite Skin Thickness

24
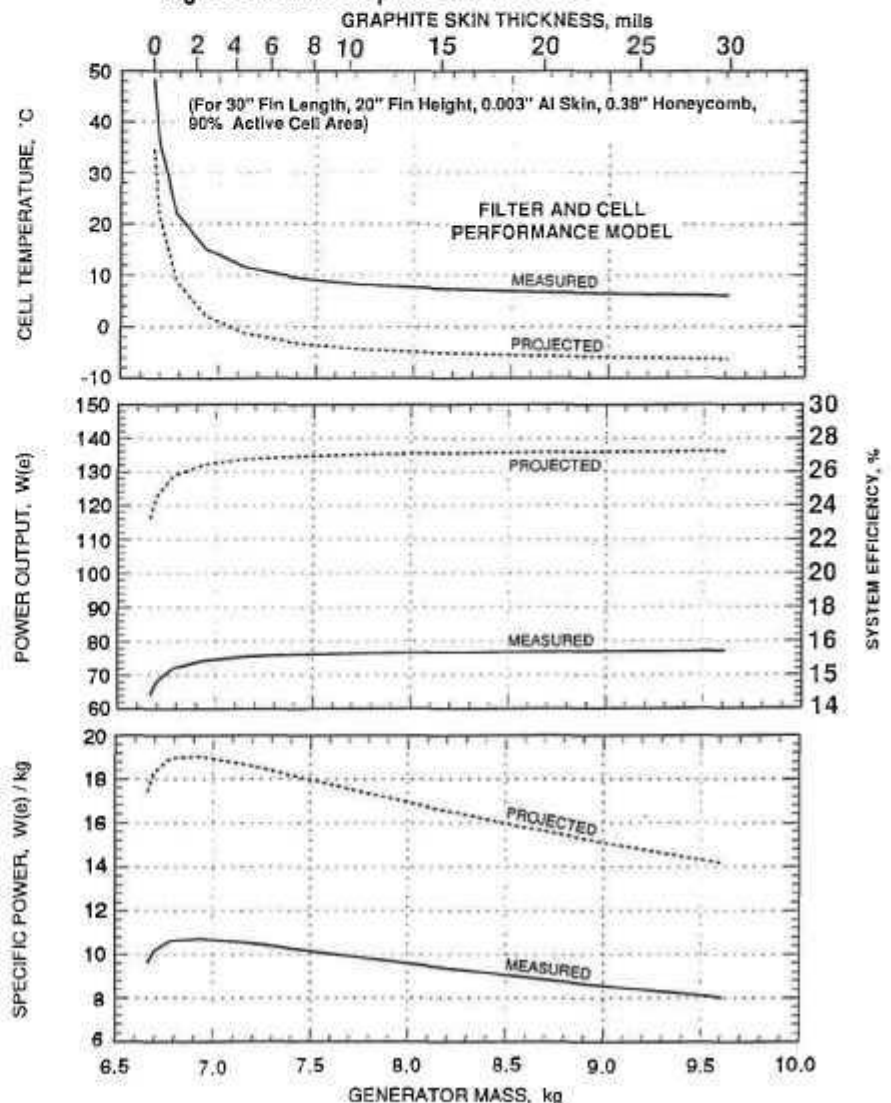
As can be seen, the projected properties (primarily the filter transmittance) have a pronounced effect on system performance. It is also noteworthy that initially the addition of the graphite skins benefits output power and efficiency significantly, but after adding a surprisingly small thickness (typically 0.005") further additions of graphite only increase the mass with little further increase of power or efficiency.

Similar analyses were carried out for fin lengths ranging from 20" to 40" and for fin tip heights of 12" and 20". The results for all cases showed similar trends, confirming the previous conclusion that the specific power of the design is maximized at a graphite skin thickness around 0.005". With thicker graphite skin, the increase in power output is quite small and is outweighed by the increased graphite mass.

The results of the parametric design studies are displayed in Figure 24 and 25. Both figures show curves representing the results of thermal, electrical, and mass analyses for fin lengths ranging 20" to 40" and fin tip heights ranging from 12" to 20", with the graphite skin thickness as the implicit variable within each curve. Each point on each curve is the result of an iterative solution of the coupled thermal and electrical analyses, using the modified thermal analysis code described earlier. All curves assume aluminum skins varying from 0.003" at the fin tip to whatever is needed near the fin root to survive a 40-g launch load without exceeding the 23 ksi allowable stress limit.

Figure 24 shows plots of cell temperature versus generator mass. For each fin size, the upper curve is based on the measured filter transmittance and PV quantum efficiency model, and the lower curve is for the projected improved filter and cell characteristics. As can be seen, the larger fins lead to very low cell temperatures, but at substantially higher mass.

Fig. 24 Effect of Fin Dimensions on Cell Temperature

25
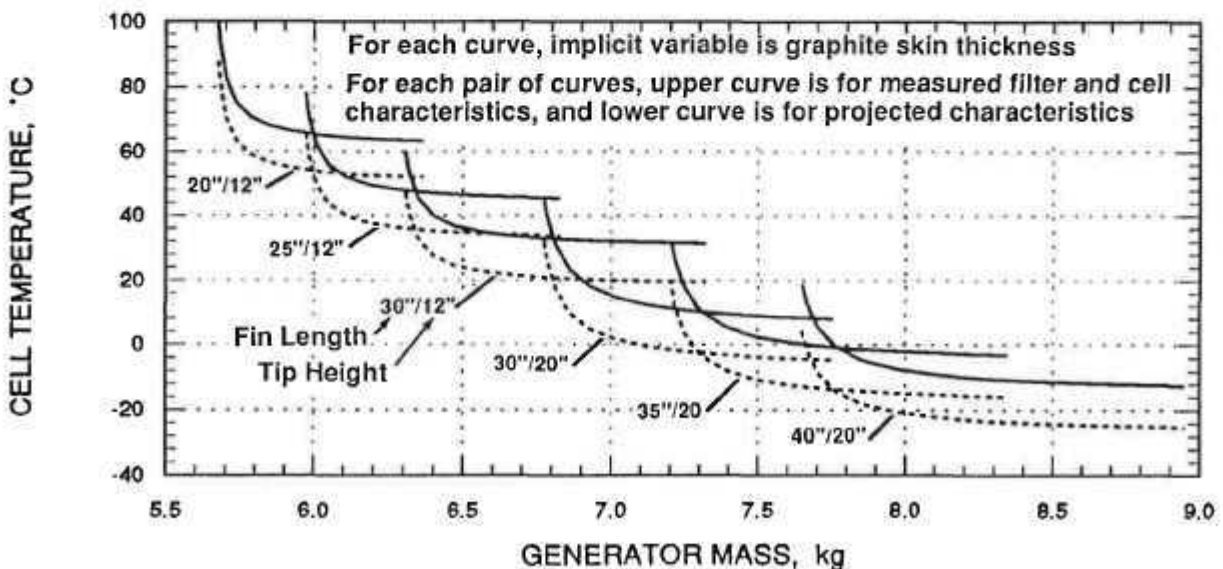
Parenthetically, it is noteworthy that the heat source temperatures were found to be virtually independent of the fin dimensions. This is because back radiation from the cold PV cells is negligible compared to the forward radiation from the hot heat source. For the measured filter and cell characteristics, the respective temperatures of the canister, heat source aeroshell, and fuel clad were 1034°C, 1062°C, and 1153°C. The corresponding temperatures with the projected improved filters and cells were 1103°C, 1128°C, and 1210°C.

The computed 1128°C aeroshell temperature for the projected filter and cell performance is somewhat above the corresponding 1100°C temperature in RTGs. But this does not matter, because the critical temperature is not the aeroshell's but the clad's. Excessive clad temperatures can lead to grain growth and embrittlement of the iridium alloy, which can lead to clad breach in case of inadvertent earth impact. The computed RTPV clad temperature of 1210°C is well below the 1300°C clad temperature in previous RTGs. This is because the presence of helium within the RTPV canister reduces the normal temperature drops between the clad and the aeroshell. In addition, a separate analysis showed that loss of helium from the canister would only result in a clad temperature rise to 1305°C, which is still within the prescribed clad temperature limit of 1330°C. This is important, because it means that the reliability and safety of the RTPV are not dependent on retaining the hermeticity of the canister.

The trade-offs between mass and performance are summarized in Figure 25. For each fin size, it presents a curve of output power and system efficiency versus generator mass, with graphite skin thickness as the implicit variable. It also shows diagonal lines of constant specific power, which identify the fin dimensions that maximize the generator's specific power.

Fig. 25 BOM Power, System Efficiency, and Specific Power Versus Generator Mass (and Implicit Graphite Thickness)
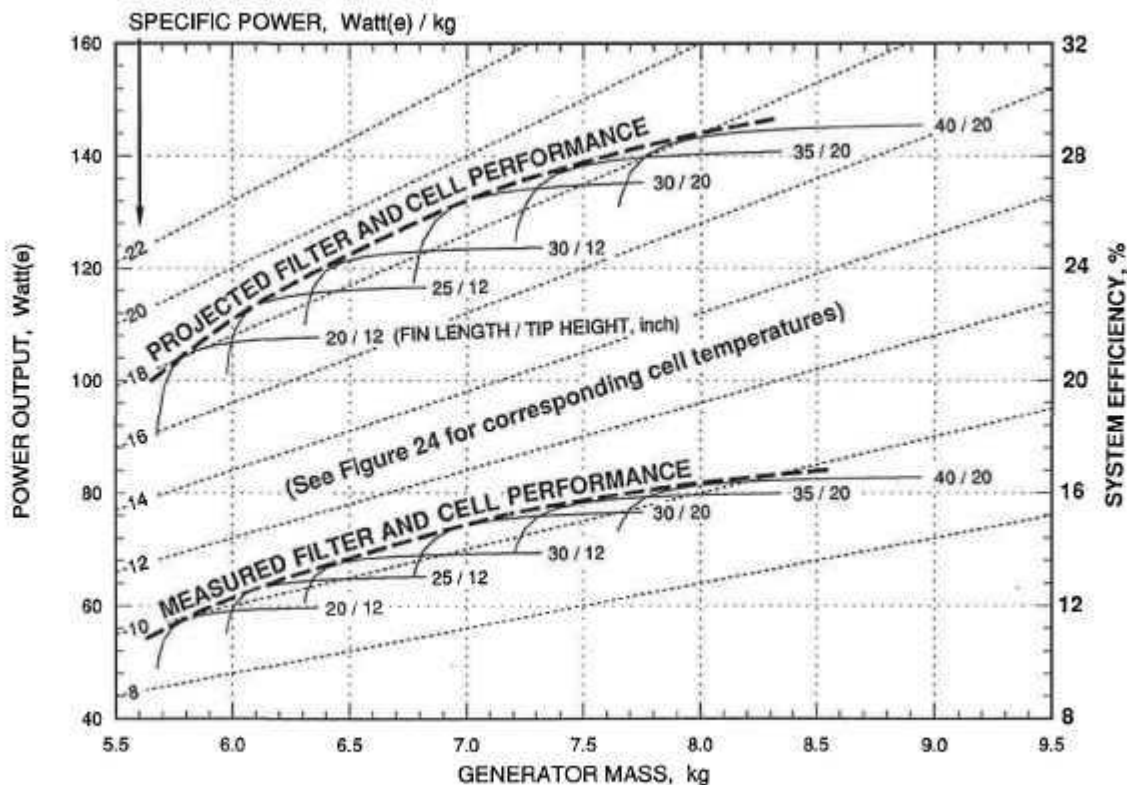
TECHNICAL CONCLUSIONS

For the measured and projected filter and cell performance models, Figure 25 shows a dashed envelope curve tangent to each family of performance curves for different fin dimensions. For each performance model, the corresponding envelope curve represents the highest specific power that can be achieved by optimizing the system's radiator geometry. For every point on the envelope, there is some combination of fin length, fin tip height, and graphite skin thickness that will achieve the indicated performance.

As can be seen, for both performance models the system's specific power is maximized with a 30" fin length and 20" fin height. But note that this optimum is quite broad. As shown, major deviations from the optimum design result in only modest reductions in specific power. Thus, the designer has wide latitude in trading off power versus mass to meet specific mission goals. For example, for the projected filter and cell performance, the BOM power could be raised from 130 watts to 145 watts by lengthening the fins from 30" to 40". As shown in Figure 25, this would increase the generator's mass from 7.2 to 8.2 kg, but would only decrease its specific power from 18.6 to 17.6 w/kg. Conversely, if desired the generator mass could be reduced from 7.2 kg to 5.7 kg by reducing the fin size. As shown in Figure 25, this would reduce the BOM power from 130 watts to 103 watts, but would only lower the generator's specific power from 18.6 to 18.0 w/kg.

Finally, we need to examine whether the large fin sizes postulated in Figure 25 could really be accommodated on the Pluto spacecraft. Figure 26 shows a trimetric view of JPL's 1993 baseline design for the PFF spacecraft. Note that they have moved the large antenna from the top to the side of the spacecraft. This frees up the space on top for mounting the optimized RTPV generator with its 30"-long fins. As shown, when the generator is rotated 45 degrees about its axis, its fins clear the antenna.

Fig. 26 Optimized RTPV Generator Mounted on Top of PFF Spacecraft

27
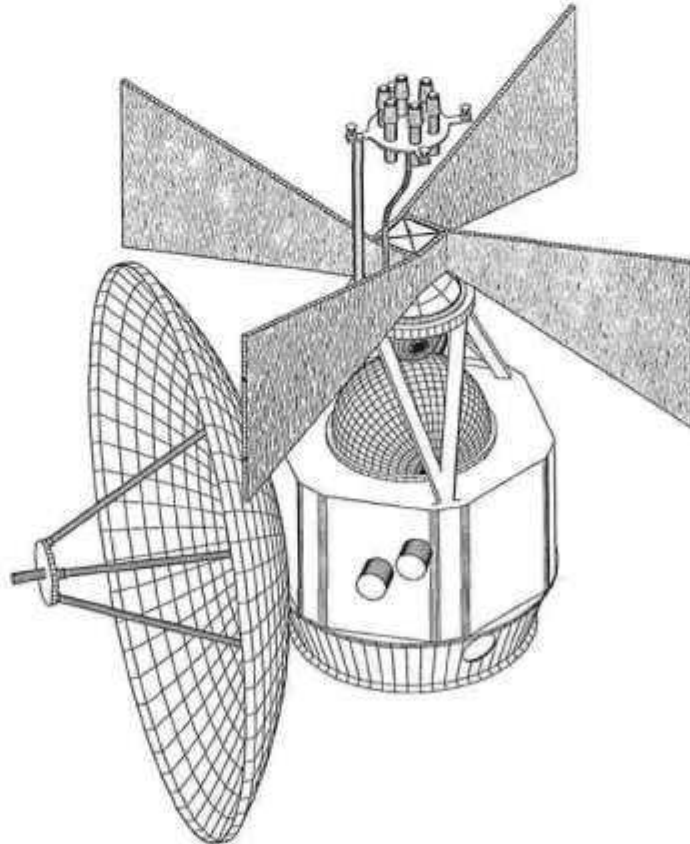
The optimum 30" fin length and 20" fin tip height were used in the RTPV design illustrations previously shown in Figures 15 and 16. For these dimensions, Table 2 presents a detailed mass breakdown, and Table 3 lists key parameters of the RTPV system for both the measured and the projected models of filter transmittance and cell quantum efficiency. For comparative purposes, the tables also list the same parameters for a recently designed RTG [8] for the Pluto Fast Flyby mission:

Table 2 Comparative Mass Breakdown (kg)

Generator	RTG	RTPV
GPHS Modules		
Fuel (PuO$_2$)	2.98	1.19
Clads (Ir)	1.17	0.47
Graphitics	3.09	1.23
Canister (Mo)	0.00	0.63
Structural Supports	1.07	0.00
Multifoil Insulation (Mo)	1.44	0.09
Converter Elements, etc.	2.15	0.17
Housing, etc.	2.90	0.53
Radiator	1.56	2.85
TOTAL	**15.36**	**7.16**

Table 3 RTG/RTPV Performance Comparison BOM

Generator	RTG	RTPV	
Performance Model	Unicouple	Measured	Projected
Generator Mass, kg	15.4	7.2	7.2
Number of Heat Source Modules	5	2	2
Thermal Power, watts	1250	500	500
Operating Temperatures, °C:			
Clad	1326	1153	1210
Aeroshell	1060	1062	1128
Canister	none	1034	1103
Converter	990/267	10.6	-2.2
Radiator Heatpipe	none	-9.3	-19.4
Output Voltage	19	30.5	32.5
Output Current, amps	4.6	2.4	4.0
Output Power, watts	87	74	130
System Efficiency, %	7.0	14.8	26.0
Specific Power, watts/kg	5.7	10.6	18.6

As shown in Table 2, the RTPV design - for both the measured and the projected performance models - offers very substantial performance improvements over the RTG. It not only meets JPL's very ambitious mass reduction goal of 9.5 kg, but at 7.2 kg it greatly exceeds it. The requirements for the costly radioisotope fuel capsules is reduced by 60%, which can result in substantial cost reductions, since historically the fuel capsules and graphitic enclosures are the dominant cost components of RTGs.

Table 3 shows that replacement of the PFF RTG with an RTPV generator having Boeing's measured filter and cell performance, even without the projected performance improvements, would roughly double the generator's efficiency and specific power. The optimized design's BOM power output of 74 watts may not be high enough to meet JPL's EOM goal of 63 watts, but could be raised above 82 watts by going to longer fins, as shown in Figure 25.

Table 3 further shows that replacement of the RTG with an RTPV having Boeing's projected filter and cell performance would roughly quadruple the generator's efficiency and triple its specific power. Moreover, it's BOM power output of 130 watts would result in an EOM output greatly in excess of JPL's 63-watt goal. This excess power capability would not be wasted, since it could be used for faster post-encounter data transmission to Earth, which would significantly reduce the mission's operating costs.

PROGRAMMATIC CONCLUSIONS

In spite of the RTPV system's potential performance superiority, the PFF project at present is likely to select the existing RTG technology because its technical maturity is much greater than that of TPV systems. There have been successful tests of gallium antimonide cells, with and without filters, but these used unoptimized cells made for the solar power program that did not reflect the full potential of the TPV converters.

Recently, Boeing conducted a preliminary scaled-down test for JPL's PFF project that endeavored to simulate the RTPV system [20]. While they reported encouraging results (13.3% measured efficiency at 1010°C) the test was hampered by constrained funding ($250K) and time limits (6 months). These limits did not permit construction and optimization of new cells and filters, and forced the use of components left over from previous programs. Those components were not only unoptimized, but the cells used came from different production batches that did not even match each other's performance, partly because of differences in contact metallization. Also, the anti-reflection coatings used were not optimized for the RTPV application. In addition, the number of available components was too small to cover more than a small fraction of the simulated heat source's surface area. Because of these limitations, the test results - while encouraging - were far from demonstrating the full potential of the RTPV system.

A concerted development effort could fairly quickly determine whether the above shortcomings could, in fact, be corrected and result in predicted BOM performance improvements. But even with such a concerted development effort, could the required lifetime of the system described in this paper be demonstrated in time for PFF's projected 2000 or 2001 launch date? Ordinarily, development of a new space power system for a long-duration mission is a very time-consuming process, because of the need for lengthy endurance tests to demonstrate long-term reliability and performance stability. But there are several aspects of this design that may greatly reduce the need for lengthy tests.

In the first place, the system is based on standard General Purpose Heat Source modules that have already been developed, safety tested, and successfully used in RTGs on previously flight program. Therefore, the costly safety test, need not be repeated, as long as the launch vehicle is not more severe than the previously used shuttle and Titan-4. This is particularly true because PFF will employ a direct flight without Earth gravity assist.

TPV converter performance can be degraded by nuclear radiation over long time. But the RTPV heat source is primarily an emitter of alpha particles, which are completely stopped by its canister. Only very small fluences of neutrons and gammas would be generated by spontaneous fissions, many orders of magnitude less than the radiation emitted by a reactor. Boeing sponsored irradiation tests conducted at Sandia indicated that the GaSb cells would experience less than 12% performance degradation in a 10-year mission [20].

Another factor that can greatly reduce the required development time is that the required TPV cells and arrays are derivatives of photovoltaic arrays developed for solar power system. Much of the technology and fabrication methods perfected for those systems over many years should also be applicable to the RTPV converter.

Most important, the lengthy endurance tests required for other power conversion systems may be greatly reduced by the unusually low operating temperatures (0 to 10°C) of the RTPV converters. Much of the lengthy testing required for other (e.g., thermoelectric) converters are dictated by the need to determine their high-temperature degradation effects over long periods. Since there is usually too little time for full-duration real-time testing (e.g., for ten years), accelerated testing must usually be employed, e.g., by using higher-than-normal operating temperatures when possible. But validation of the appropriate acceleration factors is itself a time-consuming procedure requiring lengthy tests. Fortunately, temperature-induced degradation is unlikely in TPV converters, because of their low operating temperatures.

The only high-temperature components of the RTPV system are the heat source and its canister. The stability and compatibility of the heat source components have already been demonstrated in previous RTG programs. Sublimates and outgassing products from the graphitic heat source modules could affect the TPV converters, but to prevent that the heat source is completely enclosed in a molybdenum canister coated with tungsten, whose high-temperature sublimation behavior is already well characterized and easily checked.

The above factors may minimize the need for long-term testing, and may make it possible to establish the RTPV system's flight readiness within the required PFF schedule, if their development is initiated soon. In any event, it is clear that the very substantial improvements in system efficiency and specific power that would result from successful development of radioisotope thermophotovoltaic generators by DOE and/or NASA would make such systems of great value not only for the Pluto Fast Flyby mission but also for other missions requiring small, long-lived, low-mass generators in the future.

ACKNOWLEDGMENTS

REFERENCES

[1] Dochat, George R. and Dudenhoefer, James E., "Performance Results of the Stirling Power Converter"   Proc. of the 11th Symposium on Space Nuclear Power Systems, CONF-940101, M.S. El-Genk and M.D. Hoover, eds., American Institute of Physics, New York, AIP Conference 301, 1994.

[2] Svedberg, Robert C., et al. "AMTEC Module Test Program," Proc. of the 11th Symposium on Space Nuclear Power Systems, CONF-940101, M.S. El-Genk and M.D. Hoover, eds., American Institute of Physics, New York, AIP Conference 301, 1994.

[3] Morgan, Mark D., W.E. Horne, and P.R. Brothers, "Radioisotope Thermophotovoltaic Power System Utilizing the GaSb IR Photovoltaic Cell," Proc. of the 10th Symposium on Space Nuclear Power Systems, CONF-930103, M.S. El-Genk and M.D. Hoover, eds., American Institute of Physics, New York, AIP Conference Proc. No 271, 1993.

[4] Fraas, L.M., G. Girard, J. Avery, B. Arau, V. Sundaram, A. Thompson, and J. Gee, "GaSb Booster Cells for over 30% Efficient Solar-Cell Stacks," J. Appl. Phys., 66 (8), 1989, 3866.

[5] Staehle, R., S. Weinstein, C. Salvo, and R. Terrile, "PLUTO Mission Progress Report: Lower Mass and Flight Time Through Advanced Technology," IAF-93-Q.5.410, 44th Congress of the International Astronautical Federation, Graz, Austria, 16-22 October 1993.

[6] Stern, Allen, "The Pluto Reconnaissance Flyby Mission," in Trans. of the American Geophysical Union, Vol. 74#7, February 16, 1993, p 73, 76-78.

[7] Jet Propulsion Laboratory, "Pluto Fast Flyby Program Environmental Impact Statement Supporting Study. Volume 2: Spacecraft Power Alternatives," JPL Publication No. D-10844, Jet Propulsion Laboratory, Pasadena, CA, June 14, 1993.

[8] Schock, A., "RTG Options for Pluto Fast Flyby Mission," IAF-93-R.1.425a, 44th Congress of the International Astronautical Federation, Graz Austria, 16-22 October 1993.

[9] Schock, A., "RSG Options for Pluto Fast Flyby Mission," IAF-93-R.1.425b, 44th Congress of the International Astronautical Federation, Graz Austria, 16-22 October 1993.

[10] Touloukian, Y.S. and D.P. Devitt, Thermophysical Properties of Matter, Vol 7; Thermal Radiative Properties, Metallic Elements and Alloys, 1970.

[11] Schock, A., "Design Evolution and Verification of the General-Purpose Heat Source," #809203 in Proc. of 15th Intersociety Energy Conversion Engineering Conference, held in Seattle, WA, 1980.

[12] Schock, A., "Use of Modular Heat Source Stack in RTGs," #799305 in Proc. of 14th Intersociety Energy Conversion Engineering Conference, held in Boston, MA, 1979.

[13] Denham, H.B., et. al. "NASA Advanced Radiator C-C Thin Development," Proc. of the 11th Symposium on Space Nuclear Power Systems, CONF-940101, M.S. El-Genk and M.D. Hoover, eds., American Institute of Physics, New York, 1994.

[14] Schock, A. and H. Sookiazian, "Design Optimization of RTG for Solar-Polar Mission," #799307 in Proc. of 14th Intersociety Energy Conversion Engineering Conference, held in Boston, MA, 1979.

[15] MSC/NASTRAN, Versions 65 thru 67.5. Based on NASA's NASTRAN general purpose structural analysis program. Developed and maintained by McNeal-Schwindler Corporation (MSC), CA.

[16] VibroAcoustic Payload Environment Prediction Systems (VAPEPS). Currently sponsored by NASA Lewis Research Center. The database is maintained at the VAPEPS Management Center, Jet Propulsion Laboratory, Pasadena, CA.

[17] Miner, M.A., "Cumulative Damage in Fatigue," J. Appl. Mech., 12, September 1945.

[18] Gaski, J., SINDA (System Improved Numerical Differencing Analyzed), version 1.31 5from Network Analysis Associate, Fountain Valley, CA, 1987.

[19] Little, A.D., SSPTA (Simplified Space Payload Thermal Analyzer), version 3.0/VAX, by Arthur D. Little Inc., for NASA/Goddard under Contract NAS5-27606, by Arthur D. Little Inc., Cambridge, MA, 1986.

[20] Boeing Defense and Space Group, "Thermophotovoltaic Thermal-to-Electric Con version Systems Report," Final Report to JPL Contract 959595, December 20, 1993.